Biophysical Journal Volume 105 November 2013 2323–2332

Membrane Permeation Induced by Aggregates of Human Islet Amyloid Polypeptides

Chetan Poojari,[†] Dequan Xiao,[‡] Victor S. Batista,[‡*] and Birgit Strodel[†§*]
[†]Forschungszentrum Jülich GmbH, Institute of Complex Systems: Structural Biochemistry (ICS-6), 52425 Jülich, Germany; [‡]Department of Chemistry, Yale University, New Haven, CT; and [§]Institute of Theoretical and Computational Chemistry, Heinrich Heine University Düsseldorf, 40225 Düsseldorf, Germany

ABSTRACT Several neurodegenerative diseases such as Alzheimer's and Parkinson's diseases as well as nonneuropathic diseases such as type II diabetes and atrial amyloidosis are associated with aggregation of amyloid polypeptides into fibrillar structures, or plaques. In this study, we use molecular dynamics simulations to test the stability and orientation of membrane-embedded aggregates of the human islet amyloid polypeptide (hIAPP) implicated in type II diabetes. We find that in both monolayers and bilayers of dipalmitoylphosphatidylglycerol (DPPG) hIAPP trimers and tetramers remain inside the membranes and preserve their β-sheet secondary structure. Lipid bilayer-inserted hIAPP trimers and tetramers orient inside DPPG at 60° relative to the membrane/water interface and lead to water permeation and Na^+ intrusion, consistent with ion-toxicity in islet β-cells. In particular, hIAPP trimers form a water-filled β-sandwich that induce water permeability comparable with channel-forming proteins, such as aquaporins and gramicidin-A. The predicted disruptive orientation is consistent with the amphiphilic properties of the hIAPP aggregates and could be probed by chiral sum frequency generation (SFG) spectroscopy, as predicted by the simulated SFG spectra.

INTRODUCTION

Fibrillar structures formed by protein aggregation are commonly associated with neurodegenerative diseases such as Alzheimer's, Parkinson's, and Huntington's diseases as well as nonneuropathic diseases such as type II diabetes and atrial amyloidosis (1). Fibrils readily occur in vitro and are typically composed of several twisted protofilaments that form cross β-sheets (2–5). Small oligomers along the aggregation pathway are thought to affect the integrity of cellular membranes and induce ion toxicity (6–8). However, the molecular interactions responsible for the potential membrane disruptive effect of β-sheet aggregates remain unknown (9–14). In this study, we explore these fundamental interactions through a fully atomistic study of human islet amyloid polypeptides (hIAPP) oligomers inserted in lipid bilayers, including molecular dynamics (MD) simulations of hIAPP trimers and tetramers at dipalmitoylphosphatidylglycerol (DPPG)/water interfaces. Aggregates of hIAPPs are known to be associated with type II diabetes and are thought to be detrimental to β-cells (15–17). At physiological concentrations, the 37-residue hIAPP is a neuroendocrine hormone expressed by β-cells of the pancreatic islets of Langerhans (18,19) and adopts an unstructured conformation. At higher concentrations, however, hIAPP misfolds into β-sheet-rich amyloids, as shown by solid-state NMR studies (20), electron paramagnetic resonance spectroscopy, and infrared reflection absorption spectroscopy studies (21,22). Several amino acid residues are known to be crucial for establishing hIAPP secondary structure. In particular, it has been shown that residues Ser20 to Ser29 are critical for fibril formation and toxicity (23,24).

It is known that interactions with membranes can enhance nucleation and catalyze fibril formation (25–28). Atomic force microscopy (AFM) has also revealed pore-like structures in membranes, indicating channel formation by hIAPP (29). However, it remains unclear whether hIAPP inserts into these pores by preserving its β-sheet conformation. Insight on the conformation adopted by membrane-bound hIAPP could provide understanding of the interactions leading to membrane disruption and guidelines for the development of inhibitors of hIAPP insertion into lipid bilayers, aggregation, or misfolding into β-sheets. Over the past decade several mechanisms of amyloidogenic cytotoxicity have been reported (6–8), including ion channel formation by oligomers (29,30) and alteration of membrane morphology by fibril growth at the membrane surface (9,12,31–33). It has been demonstrated that hIAPP monomers are also capable of inserting into lipid monolayers, followed by aggregation inside the membrane or with hIAPP species on the membrane surface (22,35). The initial interaction between hIAPP and negatively charged membranes is thought to be mediated by the N-terminal residues Lys1, Arg11, and His18 (27). In particular, His18 (pKa = 6.2) is thought to be essential for hIAPP/membrane interactions. In fact, at pH 7.3 a fluorescence microscopy study showed rapid increase in the intracellular calcium level after addition of $hIAPP_{1-19}$ to large unilamellar vesicles, whereas at pH 6.0 the membrane disruption ability of $hIAPP_{1-19}$ was reduced. NMR experiments showed that $hIAPP_{1-19}$ adopts a transmembrane orientation at pH 7.3, whereas at pH 6.0 the peptide orients at the micelle surface. This change in

Submitted May 11, 2013, and accepted for publication September 30, 2013.
*Correspondence: victor.batista@yale.edu or b.strodel@fz-juelich.de
Editor: Scott Feller

0006-3495/13/11/2323/10 $2.00
http://dx.doi.org/10.1016/j.bpj.2013.09.045

orientation correlates with the significantly reduced ability of $hIAPP_{1-19}$ to induce ion permeability at pH 6.0 (36).

Previous molecular simulations studies have explored α-helical hIAPP polypeptides (38,39) because hIAPP can adopt different secondary structures when exposed to different conditions (28). Another study investigated annular hIAPP structures preinserted into a zwitterionic lipid bilayer (40). The channels were seen to break into small oligomeric subunits, resembling the pore-like structures observed in AFM experiments (40). More recently, hIAPP aggregates were analyzed at the water/lipid interface by combining experimental chiral SFG spectroscopy and *ab initio* SFG simulations. It was found that hIAPP β-sheets orient with a tilting angle of 48° relative to the surface when interacting with dipalmitoylphosphoglycerol (DPPG) monolayers, an orientation that is expected to induce disruption of the lipid membrane integrity (41). However, explicit MD simulations of hIAPP β-sheets have yet to be reported. In this study, we complement earlier research of hIAPP/membrane interactions by exploring lipid bilayer-inserted hIAPP β-sheet aggregates and analyzing their orientation relative to the lipid/water interface as correlated to their disruptive effect on membrane integrity. We perform MD simulations of hIAPP trimers and tetramers in lipid layers, including hIAPP oligomers interacting with both monolayers and bilayers of DPPG. The reported simulations provide insights on the potential pathogenic effect of hIAPP, at the molecular level, particularly relevant to studies of the early stages of type II diabetes and other amyloid diseases.

METHODS

Structural models

hIAPP

The hIAPP peptide was described according to the GROMOS96 53A6 force field (42). The initial configuration of hIAPP was prepared according to the parallel U-shaped β-sheet structure determined by solid-state NMR (20). This hIAPP model is similar to the fibril structure suggested for the Alzheimer's amyloid-β peptide (Aβ) (43,44), for which a U-turn β-strand–loop–β-strand motif was independently predicted by Ma and Nussinov (45). Tycko and co-workers suggested two models for the structure of hIAPP fibrils, which only differ in the conformation of the turn region from His18 to Leu27, separating the β-strands Ala8–Val17 and Ser28–Tyr37. The N-terminal residues Lys1–Cys7 are mainly unstructured but include a Cys2–Cys7 disulfide bond, which is considered in our simulations. The configuration of the hIAPP model shown in Fig. 11 *c* of Reference (20) was preinserted into the lipid layers at 90°, relative to the membrane surface, or at 48° as defined by our previous study based on chiral SFG spectroscopy and *ab initio* quantum chemistry (41) (see Fig. S4 in Supporting Material). Fig. 1 defines the orientation of hIAPP relative to the membrane surface. The larger insertion angle in the DPPG monolayer was used to check that the results were independent of the initial configuration. The tilted orientation is consistent with the amphiphilic properties of hIAPP β-sheets as it allows the N-terminal residues to reside in the water environment and most hydrophobic residues 12–27 in the hydrophobic membrane core (46,47). Furthermore, by using the model shown Fig. 11 *c* of Reference (20), we ensure that the hydrophobic sidechains of Phe15 and Phe23 extend into the membrane core whereas Arg11 is free to interact with the anionic headgroups. The protonation state of His18, which we model uncharged, corresponds to the physiological pH.

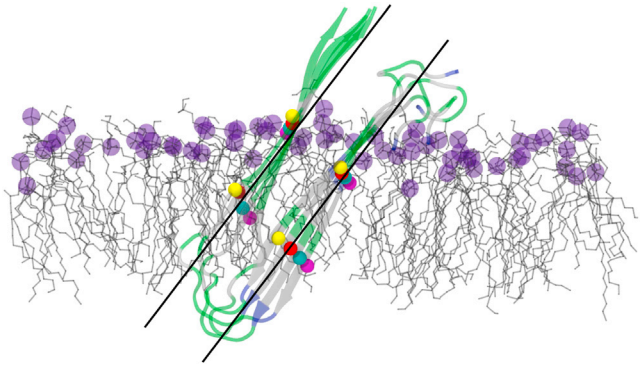

FIGURE 1 Definition of tilt angles relative to the membrane surface. To define the strand orientation, we used the C_α–C_α vector between residues Arg11 and Phe15 for the first β-strand in each peptide, and residues Leu27 and Asn31 for the second β-strand per peptide. These residues are marked by spheres in each strand. This procedure results in six different angles for the trimer and eight for the tetramer, for which the corresponding sphere colors are used in Figs. 3 and 5. The peptides are shown in New Cartoon and colored based on the physicochemical properties of the residues: blue, basic; white, hydrophobic; and green, polar. The bilayer phosphorus atoms are shown as vdW spheres in violet color. Lipid tails are shown as lines in gray color, water molecules are not shown for clarity. To see this figure in color, go online.

DPPG

A model of DPPG was built by adding two carbon atoms to each of the acyl chains of dimyristoylphosphoglycerol (DMPG) (48). The DPPG lipid was chosen to warrant comparability with previous SFG spectroscopy experiments (41). Yan and co-workers used DPPG because previous studies showed that negatively charged lipids trigger fibrillization of hIAPP at membrane surfaces (22,27) and thus can be used as a model for a cell membrane to study the mechanism for the binding of hIAPP to membrane and the aggregation of hIAPP. In the Supporting Material, details about the setup and equilibration of the DPPG monolayer (Fig. S1), and bilayer are provided. The analysis of the equilibrated DPPG bilayer yielded a highly ordered arrangement of DPPG tails (Fig. S2), with an average area of 0.6 nm^2 per lipid (Fig. S3), in agreement with previous studies of DPPG bilayers (49–51).

Molecular Dynamics Simulations

All MD simulations reported in this work were performed by using GROMACS 4.0 (52). We preinserted aggregates of hIAPP into DPPG membranes (i.e., monolayer and bilayer) by first removing the water molecules and Na^+ ions from the equilibrated model systems. Next, we inserted the hIAPP oligomers into the membranes by using the INFLATEGRO script (53), and then we solvated the systems with SPC water molecules and Na^+ counterions. The box dimensions were the same as for the corresponding membranes setups. In the case of the monolayer system, we inserted hIAPP in only one of the two monolayers in the model system. An initial equilibration under isothermal-isochoric (NVT) conditions was performed for 1 ns during which the protein heavy atoms and phosphorous atoms of the lipid headgroups were restrained with a force constant of 10,000 k J mol^{-1} nm^{-2}. The systems were then equilibrated under isothermal-isobaric (NPT) conditions for 10 ns. Long-range electrostatic interactions were calculated using the Particle Mesh-Ewald sum method with periodic boundary conditions. Van der Waals and Coulombic interaction cutoffs were set to

1.2 nm and the LINCS (linear constraint solver) algorithm was used to constrain all bond-lengths. Following equilibration, all restraints were removed and production MD runs were performed for 150 ns for each system. The time step for integration was 2 fs with coordinates and velocities saved every 20 ps for analysis.

For the analysis of the MD simulations (see Supporting Material for a detailed description), we test the structural stability and characteristics of hIAPP by calculating its root mean square deviation (RMSD) of backbone atoms and secondary structure (54), considering the probability of hydrogen bond (H-bond) formation, and clustering the sampled configurations of the last 100 ns of each trajectory (55). To quantify the orientation of the hIAPP β-sheets relative to the lipid membrane surface, we computed the tilt angle of each β-strand as illustrated in Fig. 1, yielding six angles for the trimer and eight angles for the tetramer, and calculated the mean angle (ψ) averaged over time and β-strands. Water and ion permeation across the membrane were quantified by using the g_flux and g_count utilities (56). We used the grid-based membrane analysis program GRIDMAT-MD to calculate the area per lipid and the bilayer thickness (57). To characterize the effects of the peptide on the orientational mobility of the lipid molecules, we determined the lipid tail order parameter S_{CD}. For the calculation of the osmotic permeability p_f, we followed the work of Hub et al. (58,59), who showed that by counting permeation events from equilibrium MD simulations, p_f is given as follows:

$$p_f = \frac{n_w}{2tc_w}, \tag{1}$$

where n_w denotes the number of permeation events, t is the simulation time, and c_w is the bulk water concentration.

Sum frequency generation spectrum simulations

We obtained the response function for the calculation of SFG spectra by explicitly computing the time-correlation function of the dipole moment and polarizability, giving rise to the second-order SFG response (60–62). In this study, the SFG spectrum computation is based on the analysis of vibrational normal modes using a divide-and-conquer scheme (41), where the dipole moment and polarizability changes are computed with respect to the normal coordinates. In particular, the SFG signal is calculated for the *psp* polarization setting, i.e., *p*-polarized SFG, *s*-polarized visible, and *p*-polarized infrared. The frequency-dependent *psp* intensity, $I_{psp}(\omega)$ is calculated as the magnitude squared of the frequency-dependent effective second-order susceptibility $\chi^{(2)}_{psp}(\omega)$, which results from a combination of second-order susceptibilities of all N_q normal modes, as implemented in previous studies (41,63). We model inhomogeneous and homogeneous broadening by averaging the SFG spectra computed for an ensemble of configurations sampled by MD simulations and then convoluting the contribution of each mode with a phenomenological Gaussian broadening function $g(\omega, \omega_q)$ as follows:

$$I_{psp}(\omega) = \left|\chi^{(2)}_{psp}(\omega)\right|^2 = \left|\sum_{q=1}^{N_q} g(\omega, \omega_q)\chi^{(2)}_{psp,q}\right|^2. \tag{2}$$

The *psp* effective second-order susceptibility for the q-th normal mode can be obtained from the macroscopic second-order susceptibility of the interface with tensor elements $\chi^{(2)}_{ijk,q}$ ($i, j, k = x, y$ or z, which is the lab coordinate), which are defined by the vector sum of the microscopic vibrational hyperpolarizabilities $\beta_{lmn,q}$ ($l, m, n = a, b,$ or c, which is the molecular coordinate) via an Euler transformation as follows:

$$\chi^{(2)}_{ijk,q} = N_s \sum_{l,m,n} \langle R_{il}R_{jm}R_{kn}\rangle \beta_{lmn,q}, \tag{3}$$

where N_s is the number density of the chromophores, and $\langle R_{il}R_{jm}R_{kn}\rangle$ is the average product of the Euler transformation matrix (see also Supporting Material and Fig. 2 *b* of (41)) for the projection from the molecular coordinate (a, b, and c) onto the lab coordinate (x, y, and z). $\beta_{lmn,q}$ is computed as the product of polarizability derivatives and dipole moment derivatives as follows:

$$\beta_{lmn,q} \propto \frac{\partial \alpha_{lm}}{\partial q}\frac{\partial \mu_n}{\partial q} \tag{4}$$

where $\partial\alpha_{lm}/\partial q$ and $\partial\mu_n/\partial q$ are calculated using *ab initio* quantum chemistry methods employing the Gaussian 09 program (64).

We computed hyperpolarizability elements of the parallel β-sheet structures as previously reported (20,41). The models are built by dividing the β-sheets into two β-sheet regions, the upper one including amino acid residues 8–17 and the lower one including amino acid residues 28–37. These two regions were subsequently subdivided into 16 partially overlapping tripeptide pairs (TPPs). The covalency of the dangling bonds in the fragments was completed according to the link-H atom scheme, forming amine and amide groups in the N- and C-terminal ends, respectively. The geometry of each TPP was optimized, subject to the constraint of fixed backbone dihedral angles to preserve the β-sheet configuration. Energy minimization and normal mode analysis were then performed at the density functional theory level, using the B3LYP functional and the 6-31G* basis set.

RESULTS

hIAPP β-sheets in lipid monolayers

Stability and orientation of hIAPP

The predominant transmembrane hIAPP configuration of the trimer and tetramer in a DPPG monolayer after 150 ns MD simulations are presented in Fig. 2 *a* and *b*, respectively. Both hIAPP trimer and tetramer remain inserted in the lipid layer during the whole simulation time but reorient from their initial straight insertion to a flatter position. Fig. 3 shows the tilt angle of the β-strands relative to the membrane normal, quantifying the orientation of the hIAPP model trimer and tetramer inserted in a DPPG monolayer. After the initial relaxation time of 50–75 ns, an average angle of about 40° is reached. This orientation is similar to the 48° angle predicted by chiral SFG spectroscopy and quantum chemistry calculations of hIAPP inserted in DPPG monolayers (41). The analysis of thermal fluctuations

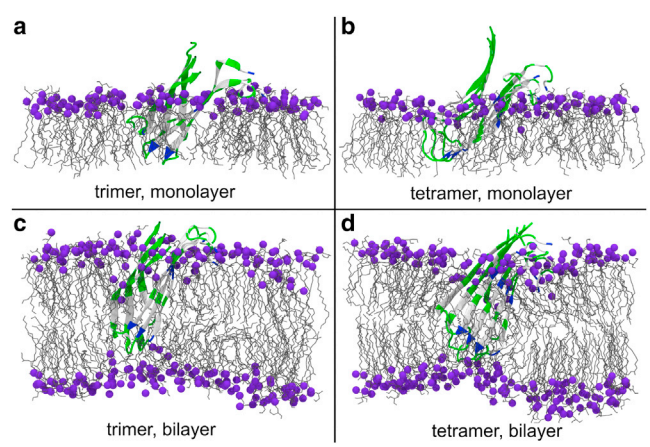

FIGURE 2 The most stable structures obtained from cluster analysis applied to the last 100 ns of the MD trajectories.

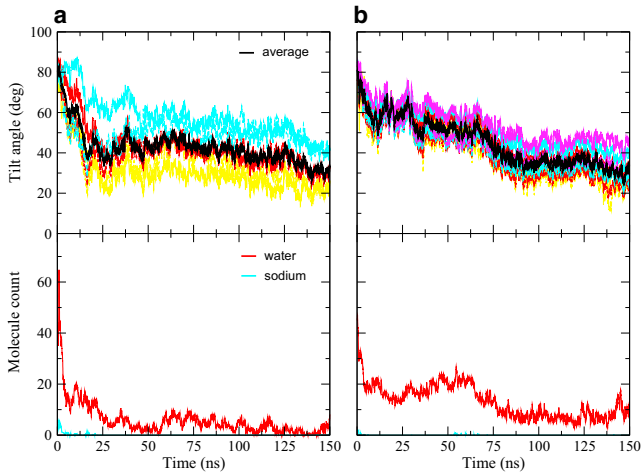

FIGURE 3 hIAPP in monolayer: (*a*) trimer and (*b*) tetramer. Top: Average (*black line*) and individual tilt angles of β-strands relative to the membrane surface. The definition of the individual angles is given in Fig. 1. Bottom: Number of water molecules and Na^+ ions inside the hydrophobic core.

shows that the angles adopted by different β-strands exhibit larger fluctuations in the more flexible trimer than in the tetramer. The trimeric β-sheet is more flexible because it has only one interior peptide and the two peptides at the edges are less stabilized by intrasheet interactions than the interior peptides.

The analysis of trajectories shows that the tilted orientation of the hIAPP β-sheets is induced by three main electrostatic interactions. First, the hIAPP aggregates tend to align Arg11 at the membrane–water interface. Second, electrostatic attractions between Lys1 and the anionic DPPG headgroups anchor the N-terminus at the membrane surface. Third, the hydrophobic mismatch between the β-sheets and the lipid tails of the monolayer force hIAPP to tilt so that the polar and charged residues remain in the aqueous environment whereas the more hydrophobic residues remain inside the membrane (Fig. 2 *a* and *b*). Consistent with these observations, we find that the RMSD of the hIAPP trimer inserted in a monolayer is ~0.7 nm, whereas the corresponding RMSD for the tetramer is only $\approx$0.45 nm (Fig. S5). Also, the average interpeptide interaction is -3248 ± 37 kJ/mol per peptide in the tetramer, whereas it is only -3104 ± 42 kJ/mol per peptide in the trimer (Table S1). The reduced interpeptide interactions in the trimer are typically compensated by peptide–lipid and peptide–water interactions. However, given the fluctuations of these energies, only the differences of the peptide–peptide interactions in the trimer and tetramer are of statistic relevance. The larger stability of the monolayer-embedded tetramer is not changed by the larger number of water molecules inside the monolayer compared with the trimer (Fig. 3). For both trimer and tetramer, water molecules embedded in the monolayer usually remain in the vicinity of polar residues between Ser20 and Ser29. Na^+ ions hardly ever insert into the lipid monolayer and when they do, they remain close to the membrane surface. The overall effect of these interactions is to preserve the almost perfect U-shape of the strand-turn-strand conformation in the tetramer but disrupt it in the trimer.

Comparison of calculated chiral SFG spectra with experiment

Fig. 4 *a* compares the experimental chiral SFG spectrum for hIAPP aggregates in a DPPG monolayer (41) with the calculated spectrum obtained for a 1:1 mixture of hIAPP tetramer and trimer. The calculated traces correspond to

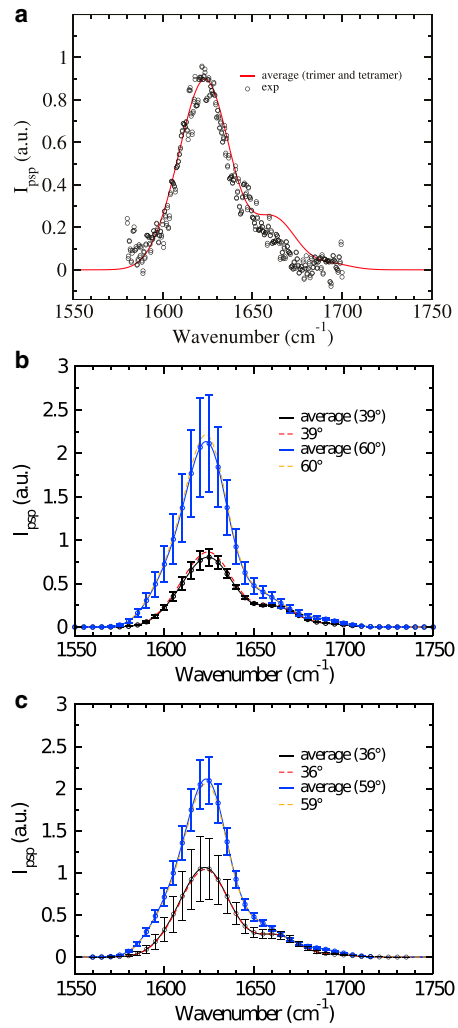

FIGURE 4 (*a*): Experimental chiral SFG spectrum for hIAPP aggregates in a DPPG monolayer (*circles*), compared with the calculated spectrum obtained for a 1:1 mixture of hIAPP tetramer and trimer (*red line*). (*b*) and (*c*): Comparisons of the calculated chiral SFG spectra for the hIAPP trimer (*b*) and tetramer (*c*) in the DPPG monolayer (*blue*) and bilayer (*black*). The error bars denote the standard deviations of the calculated spectra that are averaged for 10 orientation angles evenly distributed in the period of 50–150 ns in the molecular dynamics simulation trajectories. The average overall tilt angels are labeled for the averaged spectra. The SFG spectra with a δ-distribution at the average tilt angles are shown in the dash lines.

angle-dependent *psp* chiral SFG spectra, averaged over 75–100 ns spectra. This comparison allows for the validation of the predicted arrangement, orientation, and fluctuation of hIAPP at lipid/aqueous interfaces. Recent experiments have suggested that hIAPP β-sheet aggregates orient with an average tilt angle (ψ) of about 48° when interacting with a monolayer of DPPG lipids (41). Fig. 4 *a* shows that the spectrum of a 1:1 mixture of hIAPP trimers and tetramers inserted into DPPG lipid monolayers with an average tilt angle of about 39° and 36°, respectively, is quite similar to the spectrum obtained under typical experimental conditions. The small differences seen between the calculated and experimental spectra might suggest that monomers, dimers, and perhaps also larger aggregates (not included in the calculations) are part of the mixture probed by experiments.

Fig. 4 *b* and *c* (blue line for monolayer results) show that thermal fluctuations give rise to standard deviations in the calculated SFG spectra. Nevertheless, the spectrum obtained with a single average orientation (dash traces in Fig. 4) is very similar to the spectrum obtained by averaging all of the spectra computed along the MD trajectory (solid traces in Fig. 4). This indicates that the distributions of configurations of ψ generated by thermal fluctuations must be quite symmetric around the average value. Another interesting observation is that the amide bands (I B, centered at 1620 cm^{-1} and I A centered at 1660 cm^{-1}) are affected differently by thermal fluctuations. In fact, the standard deviation for the I B band are significantly larger than those of the I A band (error bars in Fig. 4), suggesting that the I A band is more insensitive to fluctuations in the aggregate orientation.

hIAPP β-sheets in lipid bilayers

Stability and orientation of hIAPP

The analysis of the bilayer-embedded hIAPP β-sheets shows that the hIAPP aggregates are stable during the whole simulation time of 150 ns, and insert more deeply into the hydrophobic membrane than into lipid monolayers. As shown in Fig. 2, the U-shape of the hIAPP conformation is fully preserved for the tetramer with a RMSD of only 0.35 nm (Fig. S6). The initial trimer structure is less preserved with an average RMSD of 0.65 nm, owing to the higher flexibility of the β-strands in the trimer compared with the tetramer, which enables the formation of a channel-like structure. In that structure, the β-sheets are staggered (Fig. S7) leading to the formation of a distorted yet water-filled β-sandwich, which is discussed in detail subsequently. Both trimer and tetramer adopt an orientation of about 60° as shown in Fig. 5 for the time evolution of the angles adopted by each β-strand and average orientation. To test whether the final insertion angle of hIAPP aggregates in the lipid bilayer depends on the initial orientation, we performed a 100 ns MD simulation of the trimer with an initial insertion angle of 90°. Figure S8 shows that again a stable orientation of

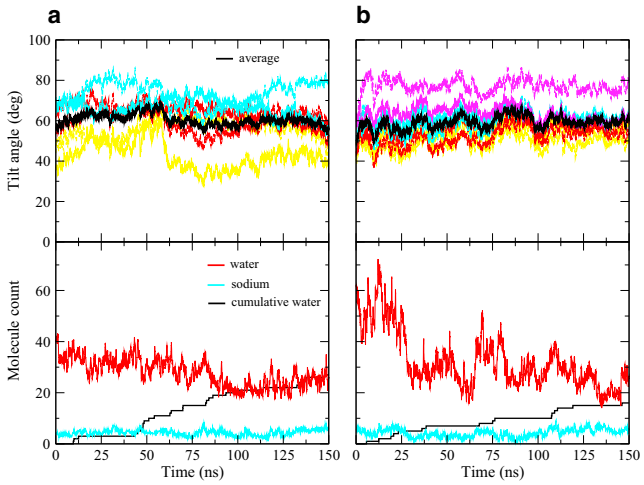

FIGURE 5 hIAPP in bilayer: (*a*) trimer and (*b*) tetramer. Top: Average (*black line*) and individual tilt angles of β-strands relative to the membrane surface. The definition of the individual angles is given in Fig. 1. Bottom: Number of water molecules and Na^+ ions inside the hydrophobic core, as well as the cumulative number of water permeation events.

about 60° is obtained within 50–60 ns, demonstrating that the DPPG bilayer allows preinserted hIAPP enough conformational freedom enabling the β-sheet aggregates to reach their equilibrium position of 60° on the nanosecond timescale and independent of the initial orientation.

The orientation of 60° allows the hIAPP β-sheets to fully span the DPPG bilayer, which is driven by peptide–lipid hydrophobic interactions and favorable contacts of hydrophilic sidechains and polar head groups on both sides of the bilayer. The interactions between hIAPP and the lipid environment are stronger for the trimer than for the tetramer, whereas the tetramer exhibits stronger peptide–peptide interactions. The time-averaged interaction energies per peptide with standard deviations are provided in Table S1. The largest difference between the trimer and tetramer energies is observed for the interactions of hIAPP with the lipid headgroups with an energy difference of ~200 kJ/mol. The tetramer structure in Fig. 2 *d* shows that one of the four hIAPP peptides is not fully inserted, which prevents its interaction with the lower headgroups and explains the diminished hIAPP–bilayer interactions in the tetramer. For both trimer and tetramer, peptide-lipid interactions are stronger than in the monolayer because hIAPP interacts with lipid headgroups in both sides of the bilayer. Electrostatic interactions between the negatively charged lipid headgroups and the positively charged amino acid residues Arg11 and Lys1 couple the N-terminal residues to the surface of the lipid bilayer (Fig. S9). Inside the bilayer the strongest interactions exist between Ser19/Asn21 and the lower headgroups, and Ser28–Asn31 and the upper headgroups. Thus, the orientation angle of 60° results from competing electrostatic interactions in the upper and lower bilayer leaflets. In fact, the sidechains of the affected polar residues are oriented such to maximally interact with the

lipid headgroups, whereas Phe15 and Phe23 extend into the hydrophobic bilayer core as in the starting model, and the polar residue His18 is in the interior of the β-sheet aggregates (Fig. S9 a).

The electrostatic interactions (Fig. S9 b) of the membrane-inserted polar residues Ser19–Asn21 and Ser28–Asn31 with the lipids disturb the bilayer arrangement, leading to the displacements of the head groups (Fig. 2) and enabling water and Na^+ ions to diffuse into the lipid bilayer. At equilibrium, we typically find 20 to 40 water molecules and as much as 5 Na^+ ions inside the DPPG bilayer, preferentially hydrating residues Ser20 to Ser29 (Fig. 5), which are known to be critical for fibril formation and toxicity (23). In particular, the trimer forms a channel-like structure across the lipid membrane and induces more water permeability than the tetramer, as quantified by the number of water molecules that translocate across the bilayer per unit time. We find that as much as 27 water molecules typically permeate the bilayer in 150 ns of dynamics when inserted by the hIAPP trimer, whereas only 16 water molecules translocate in the same amount of time when inserted by the hIAPP tetramer.

Prediction of chiral SFG spectra

The chiral SFG spectra obtained for hIAPP aggregates embedded in DPPG bilayers (close mimics of cellular membranes) are quite different from the corresponding spectra obtained for hIAPP in monolayers (black versus blue lines in Fig. 4 *b* and *c*). Note that the ratio of intensities $I(B)/I(A)$ between the B and A bands is significantly larger for the bilayer than for the monolayer. In fact, the clear shoulder observed for the A band in monolayers transforms into a very diffuse feature in the bilayer spectra. This is because of the change in orientation of the hIAPP aggregates, with an increase in the average angle ψ from 36° to 39° in the monolayer to 59° to 60° in the bilayer. These results also predict smaller standard deviations for both the amide I A-mode and B-mode regions in the lipid bilayer because the span of tilting angle around the average value of ~60° is relatively narrow. This is also observed in the comparison of the average SFG spectrum (solid lines) with the spectrum of the aggregate in the average orientation, indicating that the distribution of ψ angles does not dramatically influence the SFG spectra in this case. Hence, we anticipate that the predicted orientation of hIAPP aggregates in lipid bilayers could be confirmed by future chiral SFG spectroscopy since the spectra of hIAPP interacting with lipid bilayers or cellular membranes are quite distinct from the spectra of hIAPP interacting with lipid monolayers.

Membrane disruption by hIAPP oligomers

Effect of hIAPP on membrane ordering

hIAPP oligomers are known to disrupt the membrane integrity (6–8). However, little is known at the molecular level. Therefore, we have characterized the lipid properties as influenced by the perturbation of hIAPP aggregates. We compared the deuterium order parameter, S_{CD}, of both acyl chains 1 and 2 (sn-1 and sn-2) for lipids within 0.5 nm of hIAPP with the corresponding values for lipids that are farther away from the peptide (65,66). Figs. S10–S13 show the results of the analysis along with S_{CD} for the peptide-free DPPG membranes. The comparison reveals a disordered, fluid phase next to hIAPP. The intrinsic disorder is caused by protein-lipid interactions that tilt the lipid chains (Fig. S14), as previously observed for Aβ (65). Figs. S10–S13 also show that lipids that are $>$ 0.5 nm away from the hIAPP aggregates are largely unaffected by hIAPP-lipid interactions, implying that there is no effect on lipid ordering beyond the effect produced by the first lipid neighbor interacting directly with the hIAPP aggregate. This observation seems to be specific of the aggregate investigated and not a general feature of membrane-inserted amyloid peptides. In previous simulations, it was found that the lipid order is decreased around Aβ, but increased for the lipids further away from the peptides (65).

We note that the lipid disorder is less pronounced in the monolayer than in the bilayer because the hIAPP orientation enables the acyl chains in the monolayer to adjust better to the inserted peptides. In particular, note that the disorder because of the bulky side chains of Arg11, Phe15, and Phe23 is less extended in the monolayer than in the bilayer (Fig. S14 a vs. b). Another structural effect because of lipid disorder is the reduced thickness of the lipid bilayer next to the hIAPP aggregate. Fig. S15 shows that the bilayer is thinned by 1–2 nm in the vicinity of the peptides, whereas the lipids farther away from the peptide maintain the bilayer thickness of ~4.2 nm as in the absence of the hIAPP aggregate. We note that the reduced thickness results from favorable interactions between the protein and the lipid headgroups causing the lipids to be drawn into the membrane core (Fig. 2). These interactions also affect the area-per-lipid (APL), as shown in Figs. S16–S17. Note that the average APL in the top leaflet of the trimer is reduced by more than 0.06 nm^2 when compared with the peptide-free bilayer. In contrast, the lower leaflet remains almost unaffected. For the tetramer, however, the APL is reduced by ~0.04 nm^2 for both leaflets. These differences between the trimer and tetramer effects result from the subtle interplay between hIAPP conformation, orientation, and insertion-depth. The influence on APL also depends on the lipid layer morphology. For example, in DPPG monolayers both hIAPP trimers and tetramers increase the APL when compared with the monolayers without hIAPP. The APL increase is more significant around the hIAPP, as seen in Fig. 2.

Membrane permeation resulting from hIAPP channel formation

Fig. 6 *a* shows that the trimer loses its initial motif (i.e., the U-shaped strand-turn-strand conformation) by tilting the

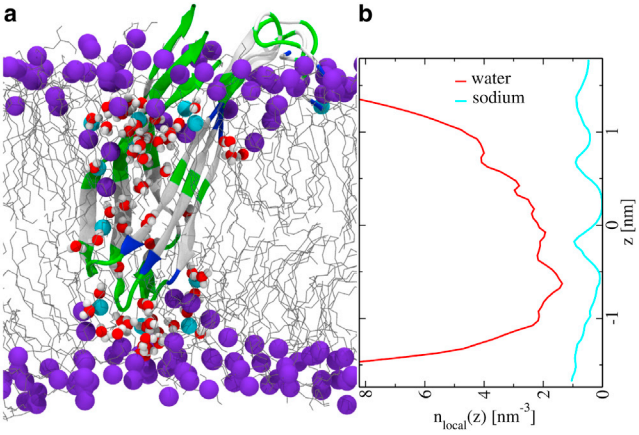

FIGURE 6 (*a*) Water channel formed by the hIAPP trimer in the DPPG bilayer. Water molecules and Na^+ (vdW spheres) inside the bilayer are shown. (*b*) Averaged particle density of water and Na^+ within the bilayer.

β-strands to form a channel-like structure in the lipid bilayer. The analysis of the trimer RMSD (Fig. S6) shows that the resulting conformation remains stable after the initial 70 ns relaxation in the lipid bilayer. The formation of the β-sandwich is driven by formation of intra- and interpeptide H-bonds in the hIAPP trimer (Fig. S7 a). Some of these H-bonds are formed between the two strands of one of the outer peptides (peptide 3 in Fig. S7), closing this side of the trimer. On the other side, however, the structure partially opens by breaking H-bonds in peptide 1. When adopting this partially open conformation, the trimer establishes a continuous transmembrane water-channel consistent with the calculated water density plot (Fig. 6 *b*). Water molecules typically enter through the open side of the sandwich and follow the channel-like structure of the hIAPP trimer on their path through the membrane (Fig. 6 *a*). The resulting water density correlates with the distribution of Na^+ ions (Fig. 6 *b*). Na^+ ions diffuse deep into the membrane and displace the lipid headgroups with them, inducing structural disorder. During the 150 ns simulation time, however, none of the Na^+ ions was able to translocate across the bilayer or exchange with Na^+ ions in the bulk. The flow of ions would be consistent with the hypothesis that hIAPP induce ion permeability leading to the observed imbalance in ion homeostasis and toxicity (29,30) that might be the cause for islet β-cell toxicity (22,26,35,67).

To test whether a higher NaCl salt concentration can induce ion translocation, we performed a 100 ns MD simulation of the hIAPP trimer in a DPPG bilayer using an initial hIAPP insertion of 48° and adding 100 mM NaCl extra to the charge balancing Na^+ ions. As in the other bilayer simulations, the β-sheet structure of the hIAPP trimer is stable and adopts an orientation of 60°. However, unlike to the salt-free simulation the U-shape conformation persists (Fig. S18 a), the water flow across the membrane is reduced, and no ions diffuse into the hydrophobic bilayer core (Fig. S18 b). The comparison of the hIAPP trimers from the simulations with and without NaCl suggests that the formation of a water-filled β-sandwich is a prerequisite for enhanced water permeation and thus ion diffusion into the bilayer. Our future studies based on nonequilibrium MD simulations will address the subtle interplay between hIAPP conformation, lipid type, salt concentration, and ion type in the process of water and ion permeation.

Osmotic permeability

In simulations without NaCl, water molecules flow through the channel formed by the hIAPP trimer from one side of the lipid bilayer to the other (Fig. S19). Although translocation can occur in 1 or 2 ns, in most cases the flux is slowed down as water molecules find stable positions inside the hIAPP/membrane complex. Therefore, the overall translocation can take as much as 20 ns before a water molecule permeates through the membrane. Most of the water molecules that stay longer inside the bilayer are preferentially found in the middle of the bilayer where the two leaflets meet. This is attributed to a free energy minimum in this region of the bilayer, for water molecules percolating through the hIAPP/bilayer (68), because of the increase of free volume in the middle of the bilayer even when there are no favorable interactions between water and hIAPP since the hIAPP residues in this region are all hydrophobic. According to Eq. 1, we can approximate the osmotic permeability p_f. With $n_w = 27$, $t = 150$ ns, and the molar concentration of water $c_w = 1$ mol/18 cm^3, we obtain $p_f = 2.7\times 10^{-15}$ cm^{-3}/s. This value is about one order of magnitude smaller than permeabilities reported (from simulation and experiment) for channel forming proteins such as aquaporins and gramicidin-A (58). However, we note that depending on the method used for determining p_f, these values can vary by almost an order of magnitude. Furthermore, the permeability we obtained here for hIAPP has to be considered as a rough estimate because it is based on only limited statistical data.

DISCUSSION AND CONCLUSIONS

Transmembrane hIAPP β-sheets

We performed MD simulations to investigate the position and orientation of β-sheet hIAPP oligomers at DPPG/water interfaces. We found that hIAPP aggregates maintain their β-sheet secondary structure and orient inside the lipid layers in a tilted, membrane disruptive, configuration that exposes hydrophobic groups to the membrane and hydrophilic residues to the aqueous phase. In lipid monolayers, the average orientation of hIAPP trimers and trimers is rather flat, with a tilt angle relative to the membrane surface of close to 40° (Fig. 2), in agreement with the overall orientation predicted by a single average configuration consistent with chiral SFG spectroscopy (41). In the lipid bilayer, hIAPP adopts a more upright orientation with a tilt angle close to 60° as a result of

electrostatic interactions of the β-sheets with lipid headgroups and counterions on both sides of the membrane (Fig. 2). Differences in the orientation of hIAPP aggregates embedded in the monolayers versus bilayers are thus because of different hydrophobic membrane widths and the balance of interactions at the peptide–bilayer/water interface. The hIAPP β-sheet structure in DPPG bilayers is similar to structures observed in simulation studies of membrane-inserted Aβ. MD simulations revealed channel conformations in lipid bilayers with truncated and full-length Aβ peptides, in which the Aβ channels are assemblies of 3 to 6 mobile β-sheet-sheet subunits each containing 2 to 6 Aβ monomers (69–76). For hIAPP, a corresponding channel model was recently developed (40), whereas for Aβ a similar pore model was independently obtained from a global optimization study of transmembrane Aβ oligomers (77).

Several aspects of the hIAPP structural models, including the hydrophilic or hydrophobic environment of several sections of the hIAPP, are consistent with experimental observations. For example, MD simulations predict that the disulfide bond between residues 2 and 7 is in the aqueous phase, consistent with experiments showing that the disulphide bond is mildly perturbed upon membrane insertion (78). In addition, residues 1–10 remain in the water compartment, enabling Lys1 to interact with the membrane surface. Furthermore, the positively charged amino-acid residue Arg11 is stabilized by the negatively charged DPPG head groups, anchoring hIAPP to the lipid/water interface in both monolayers and bilayers. Residues 20–27 remain in the lipid phase, consistent with previously work suggesting that this segment of residues must be exposed to a hydrophobic environment (46,47). In addition, His18 remains in the lipid phase during the MD simulations, consistent with the observation that in its deprotonated form (at pH 7.5) His18 induces more membrane disruption than when it is protonated at pH 6.0 (36).

Simulations of SFG spectra, averaged over orientations of the hIAPP aggregates sampled by MD simulations provide predictions that could be directly compared with experimental data. We find that a 1:1 mixture of hIAPP tetramers and timers gives a chiral SFG spectrum for hIAPP in DPPG monolayers in good agreement with experimental data. Thermal fluctuations broaden the distribution of orientations, relative to an average configuration, but do not dramatically change the resulting SFG spectra when compared with the spectrum obtained for that single average configuration. For example, for the hIAPP tetramer inserted in DPPG monolayers, spreading the tilt angle ψ from a δ-distribution at 36° to a thermal distribution in the 30° to 44° range produces at most a change of about 5% in the SFG spectra. Analogously, for the hIAPP tetramer in DPPG bilayers, spreading ψ from a δ-distribution at 59° to a distribution with a 55° to 61° range does not produce any significant effect on the resulting SFG spectrum. These findings imply that deducing the average orientation of the aggregate from comparisons of calculated and experimental chiral SFG spectra is a valid and useful approach, even when there is a distribution of orientations generated by thermal fluctuations under typical experimental conditions. At the same time, these results suggest that SFG spectroscopy could be directly applied and compared with the predicted orientations of hIAPP in DPPG bilayer, based on MD simulations.

Biomedical implications: Membrane permeability

Our MD simulations of hIAPP aggregates inserted into DPPG bilayers predict intrusion of both water and monovalent ions (e.g., Na^+) into the membrane/hIAPP complex. Water molecules form a continuous channel and permeate through the membrane, allowing Na^+ ions to diffuse into the otherwise hydrophobic membrane bilayer core. The comparative analysis of hIAPP trimers and tetramers in both DPPG monolayers and bilayers shows that changing the size of the aggregate from trimer to tetramer significantly affects the membrane permeability. In fact, only the trimer inserted in the DPPG bilayer generates a water channel because of the β-sandwich structure of the hIAPP aggregate. In contrast, the tetrameric β-sheet seems to be too stiff to enable formation of a water-filled β-sandwich. These results are particularly valuable because to the best of our knowledge this is the first study that shows channel formation by membrane-bound hIAPP oligomers, although a previous study has probed the channel activity of preformed hIAPP pores (40). It is therefore natural to expect that other amyloidogenic proteins might also be able to form channels and permeabilize the lipid bilayer.

Our estimate of the osmotic permeability p_f based on the permeation events observed for the hIAPP trimer in a DPPG bilayer, during 150 ns of MD simulations, predict that the calculated permeability coefficient is only about one order of magnitude smaller than the permeabilities reported for channel forming proteins (58). We thus conclude that membrane permeation by small hIAPP oligomers is indeed a likely mechanism for hIAPP cytotoxicity (22,26,35,67). We observe that Na^+ ions diffuse into the membrane but do not permeate from one side of the membrane to the other in 150 ns. Therefore, nonequilibrium MD trajectories are required to address whether the hIAPP β-sandwich structure allows for ion permeation. Factors influencing this process, such as membrane composition, ion type, salt concentration, and hIAPP oligomer size would have to be considered. Furthermore, nonequilibrium simulations would be required to validate the values of osmotic permeability estimated in this study, $p_f = 2.7 \times 10^{-15}$ cm^{-3}/s. Such simulations would obtain the free energy barrier for water translocation through the hIAPP channel, which could be correlated to the permeation rate (58) and enable determination of the translocation pathway as well as the various factors that might influence ion permeation.

SUPPORTING MATERIAL

Nineteen figures, References (79–80) and Supplemental information are available at http://www.biophysj.org/biophysj/supplemental/S0006-3495(13)01120-X.

The authors thank Professor Elsa C. Y. Yan for providing the experimental SFG spectrum measured for hIAPP in DPPG monolayers.

C.P. and B.S. gratefully acknowledge the Jülich Supercomputing Centre for providing the computing resources used in this work (Computing time grant JICS62). V.S.B acknowledges financial support by the National Science Foundation (Grant CHE 0911520) and supercomputer time from NERSC and from the High Performance Computing facilities at Yale University.

REFERENCES

1. Chiti, F., and C. M. Dobson. 2006. Protein misfolding, functional amyloid, and human disease. *Annu. Rev. Biochem.* 75:333–366.
2. Walsh, D. M., I. Klyubin, …, D. J. Selkoe. 2002. Naturally secreted oligomers of amyloid β protein potently inhibit hippocampal long-term potentiation *in vivo*. *Nature.* 416:535–539.
3. Kirkitadze, M. D., G. Bitan, and D. B. Teplow. 2002. Paradigm shifts in Alzheimer's disease and other neurodegenerative disorders: the emerging role of oligomeric assemblies. *J. Neurosci. Res.* 69:567–577.
4. Bucciantini, M., E. Giannoni, …, M. Stefani. 2002. Inherent toxicity of aggregates implies a common mechanism for protein misfolding diseases. *Nature.* 416:507–511.
5. Klein, W. L., W. B. Stine, Jr., and D. B. Teplow. 2004. Small assemblies of unmodified amyloid β-protein are the proximate neurotoxin in Alzheimer's disease. *Neurobiol. Aging.* 25:569–580.
6. Butterfield, S. M., and H. A. Lashuel. 2010. Amyloidogenic protein-membrane interactions: mechanistic insight from model systems. *Angew. Chem. Int. Ed. Engl.* 49:5628–5654.
7. Stefani, M. 2010. Biochemical and biophysical features of both oligomer/fibril and cell membrane in amyloid cytotoxicity. *FEBS J.* 277:4602–4613.
8. Williams, T. L., and L. C. Serpell. 2011. Membrane and surface interactions of Alzheimer's Aβ peptide—insights into the mechanism of cytotoxicity. *FEBS J.* 278:3905–3917.
9. Janson, J., R. H. Ashley, …, P. C. Butler. 1999. The mechanism of islet amyloid polypeptide toxicity is membrane disruption by intermediate-sized toxic amyloid particles. *Diabetes.* 48:491–498.
10. Anguiano, M., R. J. Nowak, and P. T. Lansbury, Jr. 2002. Protofibrillar islet amyloid polypeptide permeabilizes synthetic vesicles by a pore-like mechanism that may be relevant to type II diabetes. *Biochemistry.* 41:11338–11343.
11. Porat, Y., S. Kolusheva, …, E. Gazit. 2003. The human islet amyloid polypeptide forms transient membrane-active prefibrillar assemblies. *Biochemistry.* 42:10971–10977.
12. Kayed, R., Y. Sokolov, …, C. G. Glabe. 2004. Permeabilization of lipid bilayers is a common conformation-dependent activity of soluble amyloid oligomers in protein misfolding diseases. *J. Biol. Chem.* 279:46363–46366.
13. Demuro, A., E. Mina, …, C. G. Glabe. 2005. Calcium dysregulation and membrane disruption as a ubiquitous neurotoxic mechanism of soluble amyloid oligomers. *J. Biol. Chem.* 280:17294–17300.
14. Ritzel, R. A., J. J. Meier, …, P. C. Butler. 2007. Human islet amyloid polypeptide oligomers disrupt cell coupling, induce apoptosis, and impair insulin secretion in isolated human islets. *Diabetes.* 56:65–71.
15. Clark, A., C. A. Wells, …, R. C. Turner. 1988. Islet amyloid, increased A-cells, reduced B-cells and exocrine fibrosis: quantitative changes in the pancreas in type 2 diabetes. *Diabetes Res.* 9:151–159.
16. Hull, R. L., G. T. Westermark, …, S. E. Kahn. 2004. Islet amyloid: a critical entity in the pathogenesis of type 2 diabetes. *J. Clin. Endocrinol. Metab.* 89:3629–3643.
17. Kahn, S. E., S. Andrikopoulos, and C. B. Verchere. 1999. Islet amyloid: a long-recognized but underappreciated pathological feature of type 2 diabetes. *Diabetes.* 48:241–253.
18. Höppener, J. W., C. Oosterwijk, …, C. J. Lips. 1994. Molecular physiology of the islet amyloid polypeptide (IAPP)/amylin gene in man, rat, and transgenic mice. *J. Cell. Biochem.* 55 (*Suppl*):39–53.
19. Kahn, S. E., D. A. D'Alessio, …, D. Porte, Jr. 1990. Evidence of cosecretion of islet amyloid polypeptide and insulin by beta-cells. *Diabetes.* 39:634–638.
20. Luca, S., W. M. Yau, …, R. Tycko. 2007. Peptide conformation and supramolecular organization in amylin fibrils: constraints from solid-state NMR. *Biochemistry.* 46:13505–13522.
21. Jayasinghe, S. A., and R. Langen. 2004. Identifying structural features of fibrillar islet amyloid polypeptide using site-directed spin labeling. *J. Biol. Chem.* 279:48420–48425.
22. Lopes, D. H. J., A. Meister, …, R. Winter. 2007. Mechanism of islet amyloid polypeptide fibrillation at lipid interfaces studied by infrared reflection absorption spectroscopy. *Biophys. J.* 93:3132–3141.
23. Westermark, P., U. Engström, …, C. Betsholtz. 1990. Islet amyloid polypeptide: pinpointing amino acid residues linked to amyloid fibril formation. *Proc. Natl. Acad. Sci. USA.* 87:5036–5040.
24. Jaikaran, E. T., C. E. Higham, …, P. E. Fraser. 2001. Identification of a novel human islet amyloid polypeptide beta-sheet domain and factors influencing fibrillogenesis. *J. Mol. Biol.* 308:515–525.
25. Jayasinghe, S. A., and R. Langen. 2005. Lipid membranes modulate the structure of islet amyloid polypeptide. *Biochemistry.* 44:12113–12119.
26. Knight, J. D., and A. D. Miranker. 2004. Phospholipid catalysis of diabetic amyloid assembly. *J. Mol. Biol.* 341:1175–1187.
27. Knight, J. D., J. A. Hebda, and A. D. Miranker. 2006. Conserved and cooperative assembly of membrane-bound alpha-helical states of islet amyloid polypeptide. *Biochemistry.* 45:9496–9508.
28. Sparr, E., M. F. M. Engel, …, J. A. Killian. 2004. Islet amyloid polypeptide-induced membrane leakage involves uptake of lipids by forming amyloid fibers. *FEBS Lett.* 577:117–120.
29. Quist, A., I. Doudevski, …, R. Lal. 2005. Amyloid ion channels: a common structural link for protein-misfolding disease. *Proc. Natl. Acad. Sci. USA.* 102:10427–10432.
30. Mirzabekov, T. A., M. C. Lin, and B. L. Kagan. 1996. Pore formation by the cytotoxic islet amyloid peptide amylin. *J. Biol. Chem.* 271:1988–1992.
31. Lorenzo, A., B. Razzaboni, …, B. A. Yankner. 1994. Pancreatic islet cell toxicity of amylin associated with type-2 diabetes mellitus. *Nature.* 368:756–760.
32. O'Brien, T. D., P. C. Butler, …, N. L. Eberhardt. 1995. Human islet amyloid polypeptide expression in COS-1 cells. A model of intracellular amyloidogenesis. *Am. J. Pathol.* 147:609–616.
33. Hiddinga, H. J., and N. L. Eberhardt. 1999. Intracellular amyloidogenesis by human islet amyloid polypeptide induces apoptosis in COS-1 cells. *Am. J. Pathol.* 154:1077–1088.
34. Reference deleted in proof.
35. Engel, M. F. M., H. Yigittop, …, J. Antoinette Killian. 2006. Islet amyloid polypeptide inserts into phospholipid monolayers as monomer. *J. Mol. Biol.* 356:783–789.
36. Brender, J. R., K. Hartman, …, A. Ramamoorthy. 2008. A single mutation in the nonamyloidogenic region of islet amyloid polypeptide greatly reduces toxicity. *Biochemistry.* 47:12680–12688.
37. Reference deleted in proof.
38. Zhang, Y., Y. Luo, …, G. Wei. 2012. Lipid interaction and membrane perturbation of human islet amyloid polypeptide monomer and dimer by molecular dynamics simulations. *PLoS ONE.* 7:e38191.

39. Duan, M., J. Fan, and S. Huo. 2012. Conformations of islet amyloid polypeptide monomers in a membrane environment: implications for fibril formation. *PLoS ONE.* 7:e47150.

40. Zhao, J., Y. Luo, …, J. Zheng. 2012. Probing ion channel activity of human islet amyloid polypeptide (amylin). *Biochim. Biophys. Acta.* 1818:3121–3130.

41. Xiao, D., L. Fu, …, E. C. Yan. 2012. Amphiphilic adsorption of human islet amyloid polypeptide aggregates to lipid/aqueous interfaces. *J. Mol. Biol.* 421:537–547.

42. Oostenbrink, C., A. Villa, …, W. F. van Gunsteren. 2004. A biomolecular force field based on the free enthalpy of hydration and solvation: the GROMOS force-field parameter sets 53A5 and 53A6. *J. Comput. Chem.* 25:1656–1676.

43. Lührs, T., C. Ritter, …, R. Riek. 2005. 3D structure of Alzheimer's amyloid-β(1–42) fibrils. *Proc. Natl. Acad. Sci. USA.* 102:17342–17347.

44. Petkova, A. T., W. M. Yau, and R. Tycko. 2006. Experimental constraints on quaternary structure in Alzheimer's β-amyloid fibrils. *Biochemistry.* 45:498–512.

45. Ma, B., and R. Nussinov. 2002. Stabilities and conformations of Alzheimer's β -amyloid peptide oligomers (Abeta (16-22), Abeta (16-35), and Abeta (10-35)): Sequence effects. *Proc. Natl. Acad. Sci. USA.* 99:14126–14131.

46. Goldsbury, C., K. Goldie, …, U. Aebi. 2000. Amyloid fibril formation from full-length and fragments of amylin. *J. Struct. Biol.* 130:352–362.

47. Madine, J., E. Jack, …, D. A. Middleton. 2008. Structural insights into the polymorphism of amyloid-like fibrils formed by region 20–29 of amylin revealed by solid-state NMR and X-ray fiber diffraction. *J. Am. Chem. Soc.* 130:14990–15001.

48. Piggot, T. J., D. A. Holdbrook, and S. Khalid. 2011. Electroporation of the E. coli and S. Aureus membranes: molecular dynamics simulations of complex bacterial membranes. *J. Phys. Chem. B.* 115:13381–13388.

49. Kaznessis, Y. N., S. Kim, and R. G. Larson. 2002. Simulations of zwitterionic and anionic phospholipid monolayers. *Biophys. J.* 82:1731–1742.

50. Zaraiskaya, T., and K. R. Jeffrey. 2005. Molecular dynamics simulations and 2H NMR study of the GalCer/DPPG lipid bilayer. *Biophys. J.* 88:4017–4031.

51. Pabst, G., S. L. Grage, …, A. Hickel. 2008. Membrane thickening by the antimicrobial peptide PGLa. *Biophys. J.* 95:5779–5788.

52. Hess, B., C. Kutzner, …, E. Lindahl. 2008. GROMACS 4: algorithms for highly efficient, load-balanced, and scalable molecular simulation. *J. Chem. Theory Comput.* 4:435–447.

53. Kandt, C., W. L. Ash, and D. P. Tieleman. 2007. Setting up and running molecular dynamics simulations of membrane proteins. *Methods.* 41:475–488.

54. Kabsch, W., and C. Sander. 1983. Dictionary of protein secondary structure: pattern recognition of hydrogen-bonded and geometrical features. *Biopolymers.* 22:2577–2637.

55. Daura, X., K. Gademann, …, A. Mark. 1999. Peptide folding: when simulation meets experiment. *Angew. Chem. Int. Ed.* 38:236–240.

56. Beckstein, O., and M. S. P. Sansom. 2004. The influence of geometry, surface character, and flexibility on the permeation of ions and water through biological pores. *Phys. Biol.* 1:42–52.

57. Allen, W. J., J. A. Lemkul, and D. R. Bevan. 2009. GridMAT-MD: a grid-based membrane analysis tool for use with molecular dynamics. *J. Comput. Chem.* 30:1952–1958.

58. Hub, J. S., H. Grubmüller, and B. L. de Groot. 2009. Dynamics and energetics of permeation through aquaporins. What do we learn from molecular dynamics simulations? *In* Aquaporins, Vol. 190, Handbook of Experimental Pharmacology. E. Beitz, editor. Springer, Berlin, pp. 57–76.

59. Hub, J. S., F. K. Winkler, …, B. L. de Groot. 2010. Potentials of mean force and permeabilities for carbon dioxide, ammonia, and water flux across a Rhesus protein channel and lipid membranes. *J. Am. Chem. Soc.* 132:13251–13263.

60. Ishiyama, T., and A. Morita. 2009. Analysis of anisotropic local field in sum frequency generation spectroscopy with the charge response kernel water model. *J. Chem. Phys.* 131:244714.

61. Nagata, Y., and S. Mukamel. 2010. Vibrational sum-frequency generation spectroscopy at the water/lipid interface: molecular dynamics simulation study. *J. Am. Chem. Soc.* 132:6434–6442.

62. Pieniazek, P. A., C. J. Tainter, and J. L. Skinner. 2011. Interpretation of the water surface vibrational sum-frequency spectrum. *J. Chem. Phys.* 135:044701.

63. Moad, A. J., and G. J. Simpson. 2004. A unified treatment of selection rules and symmetry relations for sum-frequency and second harmonic spectroscopies. *J. Phys. Chem. B.* 108:3548–3562.

64. Frisch, M., G. Trucks, …, J. Farkas. 2009. Gaussian 09, Revision A.01. Gaussian, Wallingford, CT.

65. Poojari, C., A. Kukol, and B. Strodel. 2013. How the amyloid-β peptide and membranes affect each other: an extensive simulation study. *Biochim. Biophys. Acta. (Biomembr.).* 1828:327–339.

66. Poojari, P., and B. Strodel. 2013. Stability of transmembrane amyloid β-peptide and membrane integrity tested by molecular modeling of site-specific Aβ42 mutations. *PLoS ONE.* In press.

67. Lee, C.-C., Y. Sun, and H. W. Huang. 2012. How type II diabetes-related islet amyloid polypeptide damages lipid bilayers. *Biophys. J.* 102:1059–1068.

68. Saito, H., and W. Shinoda. 2011. Cholesterol effect on water permeability through DPPC and PSM lipid bilayers: a molecular dynamics study. *J. Phys. Chem. B.* 115:15241–15250.

69. Jang, H., J. Zheng, …, R. Nussinov. 2008. New structures help the modeling of toxic amyloidbeta ion channels. *Trends Biochem. Sci.* 33:91–100.

70. Jang, H., J. Zheng, and R. Nussinov. 2007. Models of beta-amyloid ion channels in the membrane suggest that channel formation in the bilayer is a dynamic process. *Biophys. J.* 93:1938–1949.

71. Jang, H., F. T. Arce, …, R. Nussinov. 2009. Misfolded amyloid ion channels present mobile beta-sheet subunits in contrast to conventional ion channels. *Biophys. J.* 97:3029–3037.

72. Jang, H., F. T. Arce, …, R. Lal. 2011. Antimicrobial protegrin-1 forms amyloid-like fibrils with rapid kinetics suggesting a functional link. *Biophys. J.* 100:1775–1783.

73. Capone, R., H. Jang, …, R. Lal. 2012. Probing structural features of Alzheimer's amyloid-β pores in bilayers using site-specific amino acid substitutions. *Biochemistry.* 51:776–785.

74. Arce, F. T., H. Jang, …, R. Lal. 2011. Polymorphism of amyloid β peptide in different environments: implications for membrane insertion and pore formation. *Soft Matter.* 7:5267–5273.

75. Capone, R., H. Jang, …, R. Lal. 2012. All-D-enantiomer of β-amyloid peptide forms ion channels in lipid bilayers. *J. Chem. Theory Comput.* 8:1143–1152.

76. Connelly, L., H. Jang, …, R. Lal. 2012. Atomic force microscopy and MD simulations reveal pore-like structures of all-D-enantiomer of Alzheimer's β-amyloid peptide: relevance to the ion channel mechanism of AD pathology. *J. Phys. Chem. B.* 116:1728–1735.

77. Strodel, B., J. W. Lee, …, D. J. Wales. 2010. Transmembrane structures for Alzheimer's Aβ(1-42) oligomers. *J. Am. Chem. Soc.* 132:13300–13312.

78. Khemtémourian, L., M. F. Engel, …, J. A. Killian. 2010. The role of the disulfide bond in the interaction of islet amyloid polypeptide with membranes. *Eur. Biophys. J.* 39:1359–1364.

79. Martínez, L., R. Andrade, …, J. M. Martínez. 2009. PACKMOL: a package for building initial configurations for molecular dynamics simulations. *J. Comput. Chem.* 30:2157–2164.

80. Feller, S. E., Y. Zhang, and R. W. Pastor. 1995. Computer simulation of liquid/liquid interfaces. II. Surface tension-area dependence of a bilayer and monolayer. *J. Chem. Phys.* 103:10267–10276.

Supporting material

Membrane permeation induced by aggregates of human islet amyloid polypeptides

Chetan Poojari
Forschungszentrum Jülich GmbH,
Institute of Complex Systems: Structural Biochemistry (ICS-6),
52425 Jülich, Germany

Dequan Xiao
Department of Chemistry,
Yale University
New Haven, CT 06520, USA

Victor S. Batista*
Department of Chemistry,
Yale University
New Haven, CT 06520, USA

Birgit Strodel*
Forschungszentrum Jülich GmbH,
Institute of Complex Systems: Structural Biochemistry (ICS-6),
52425 Jülich, Germany

Institute of Theoretical and Computational Chemistry,
Heinrich Heine University Düsseldorf, 40225 Düsseldorf, Germany

*Corresponding Authors: victor.batista@yale.edu; b.strodel@fz-juelich.de

DPPG bilayer setup.
The PACKMOL package (1) was used to build a DPPG bilayer patch of 256 lipids with 128 lipids in each leaflet. The DPPG bilayer patch was solvated with 9,888 SPC water molecules and 256 Na^+ ions were added to neutralize the negatively charged DPPG molecules with each ion taking the place of a randomly chosen water molecule. The resulting DPPG bilayer system contained 42,208 atoms in a simulation box with dimensions of 8.6 × 8.6 × 8.0 nm^3 . The system was simulated for 100 ns at 323 K using a Nose-Hoover thermostat to regulate the temperature along with semiisotropic Parrinello-Rahman pressure coupling. The bilayer normal z-direction and xy-plane were coupled separately with a time constant of 2 ps maintaining a constant pressure of 1 bar independently in all directions. An isothermal compressibility of 4.5 × 105 bar^{-1} was applied in all box dimensions.

DPPG monolayer setup.
DPPG monolayers were built from the DPPG bilayer system by separating the two leaflets (2). The lower leaflet was moved in the positive z-direction while the upper leaflet was displaced in the negative *z*-direction until the separation between both membrane surfaces was 5.4 nm. Thus, the resulting system consisted of two monolayers with 128 DPPG lipids per layer separated by a central layer, which was filled with 11,389 SPC water molecules and 256 Na^+ ions. The complete DPPG monolayer system included 47,271 atoms within the simulation box of dimensions 8.6 × 8.6 × 16.0 nm^3. The large box length in the *z*-direction is necessary to create a vacuum region above and below the lipid tails of the upper and lower monolayer, respectively, to avoid any interactions between tail atoms of the two monolayers. A representative configuration of the DPPG monolayer system is shown in Fig. S1. This system was simulated for 100 ns at 323 K using a Nose-Hoover thermostat to regulate the temperature with a time constant of 1 ps. To control the pressure, a surface tension pressure coupling scheme with a time constant of 4 ps was employed (3). An isothermal compressibility of 4.5 × 105 bar^{-1} was applied in the lateral *x* and *y*-directions, while the compressibility was set to zero in the *z*-direction to prevent box contraction.

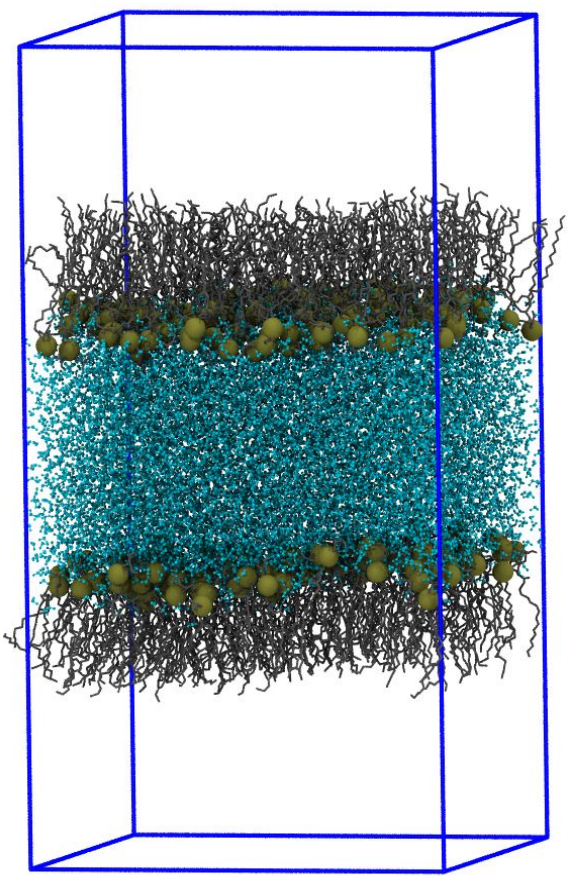

Figure S1: Snapshot showing the DPPG monolayer-water system. The monolayer phosphorus atoms (tan) are shown as van der Waals spheres, lipid tails (gray) as licorice and water molecules (blue) are shown as CPK. The simulation box is drawn to emphasize the empty space representing the air above and below the lipid tails in the upper and lower monolayer, respectively.

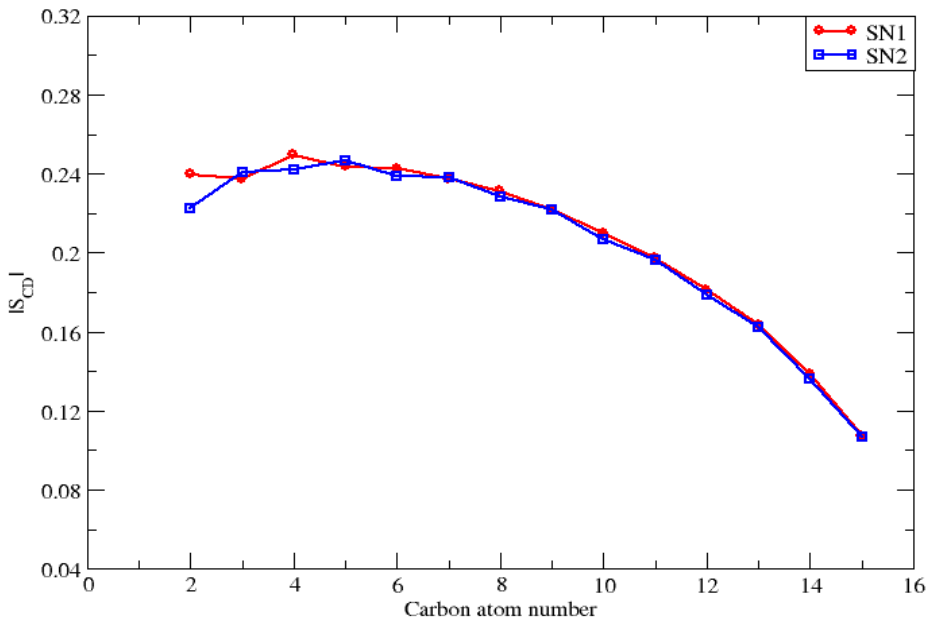

Figure S2: Time-averaged order parameter $|S_{CD}|$ of the sn-1 and sn-2 lipid chains obtained from a 100 ns MD simulation of a peptide-free DPPG bilayer.

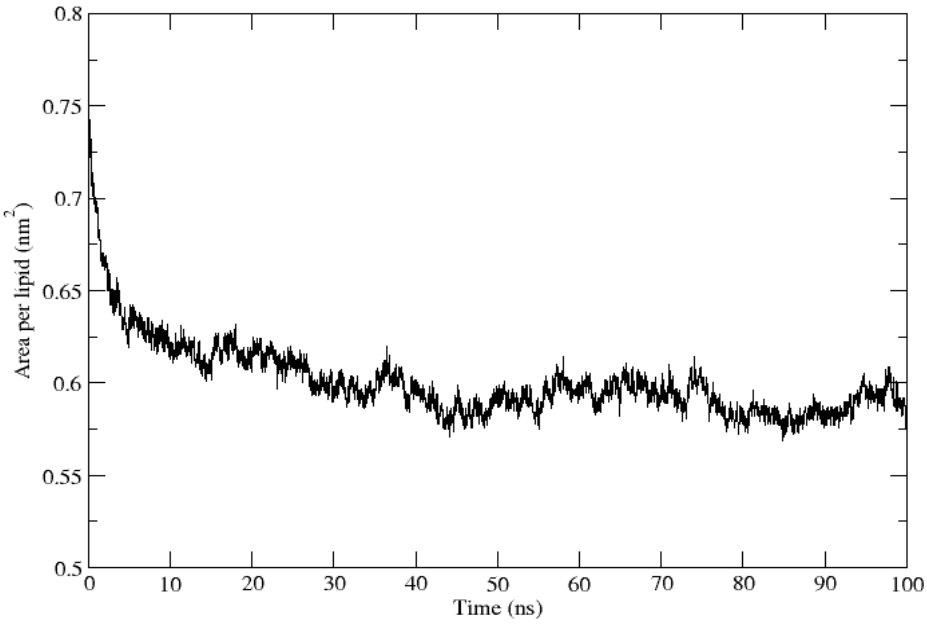

Figure S3: Area per lipid as a function of time as obtained during a 100 ns MD simulation of a peptide-free DPPG lipid bilayer.

Analysis of the MD simulations

The structural stability of hIAPP was tested by calculating the root mean square deviation (RMSD) of backbone atoms. The secondary structure of hIAPP was analyzed using the DSSP (dictionary of protein secondary structure) method (3). The probability of hydrogen bond (H-bond) formation was considered based on a cutoff distance of 0.36 nm between donor and acceptor atoms and a cutoff angle off linearity of 30°. For the representation of the predominant transmembrane hIAPP oligomers, we clustered the sampled configurations of the last 100 ns of each trajectory using the method by Daura *et al*. (4) with a 0.2 nm cutoff for the backbone atoms. To quantify the orientation of the hIAPP β-sheets relative to the lipid membrane surface we computed the tilt angle of β-strands using the GROMACS analysis tool g_bundle. Here, each β-strand was considered separately, yielding 6 angles for the trimer and 8 for the tetramer. To define the strand orientation we used the Cα –Cα vector between residues Arg11 and Phe15 for the first β- strand in each peptide, and residues Leu27 and Asn31 for the second β-strand per peptide. Subsequently, we calculated the mean angle averaged over time and β-strands. Water and ion permeation across the membrane were quantified by using the g_flux and g_count utilities (5). We used the grid-based membrane analysis tool GRIDMAT-MD to calculate the area per lipid and the bilayer thickness (6). For the bilayer thickness we report phosphate-to-phosphate distances. To characterize the effects of the peptide on the orientational mobility of the lipid molecules we calculated the lipid tail order parameter S_{CD} defined as

$$S_{CD} = ½ <3 \cos^2 \theta - 1 >,$$

where the angular brackets indicate average over lipids and over time and θ is the angle between the C–H bond vector (or C–D bond vector in the experiment) relative to the bilayer normal. For the calculation of the osmotic permeability p_f we followed the work of Hub *et al*. (7, 8), who showed that by counting permeation events from equilibrium MD simulations p_f is given as

$$p_f = n_w / 2tc_w ,$$

where n_w denotes the number of permeation events, t is the simulation time and c_w is the bulk water concentration. The factor of 1/2 corrects for the permeation events counted in both directions during the simulation, while pf is defined from the flux in one direction in response to a concentration gradient.

Sum frequency generation spectrum calculations

The *psp* effective second-order susceptibility for the *q*-th normal mode is

$$c^{(2)}_{psp,q} = L_{zyx} c^{(2)}_{zyx,q} - L_{xyz} c^{(2)}_{xyz,q} ,$$

where L_{zyx} and L_{xyz} are the Fresnel factors (9), and $\chi^{(2)}_{ijk,q}$ (*i*, *j*, *k* = *x*, *y* or *z*, which is the lab coordinate) is the tensor element of the macroscopic second-order susceptibility of the interface. $\chi^{(2)}_{ijk,q}$ is defined by the vector sum of the microscopic vibrational hyperpolarizability for *q*-th normal mode $\beta_{lmn,q}$ (*l*, *m*, *n* = *a*, *b* or *c*, which is the molecular coordinate) *via* an Euler transformation:

$$c^{(2)}_{ijk,q} = N_s \sum_{l,m,n} \langle R_{il} R_{jm} R_{kn} \rangle \beta_{lmn,q} ,$$

where N_s is the number density of the chromophores, and $\langle R_{il} R_{jm} R_{kn} \rangle$ is the average product of the Euler transformation matrix for the projection from the molecular coordinate (*a*, *b* and *c*) onto the lab coordinate (*x*, *y*, and *z*). $\langle R_{il} R_{jm} R_{kn} \rangle$ is a function of the Euler angles ϕ, θ, and ψ that are defined in Fig. 2b of Ref. (10):

$$R = \begin{pmatrix} \cos(\varphi)\cos(\theta)\cos(\psi) - \sin(\varphi)\sin(\psi) & \cos(\varphi)\cos(\theta)\sin(\psi) + \sin(\varphi)\cos(\psi) & -\cos(\varphi)\sin(\theta) \\ -\sin(\varphi)\cos(\theta)\cos(\psi) - \cos(\varphi)\sin(\psi) & -\sin(\varphi)\cos(\theta)\sin(\psi) + \cos(\varphi)\cos(\psi) & \sin(\varphi)\sin(\theta) \\ \sin(\theta)\cos(\psi) & \sin(\theta)\sin(\psi) & \cos(\theta) \end{pmatrix}$$

Supporting figures

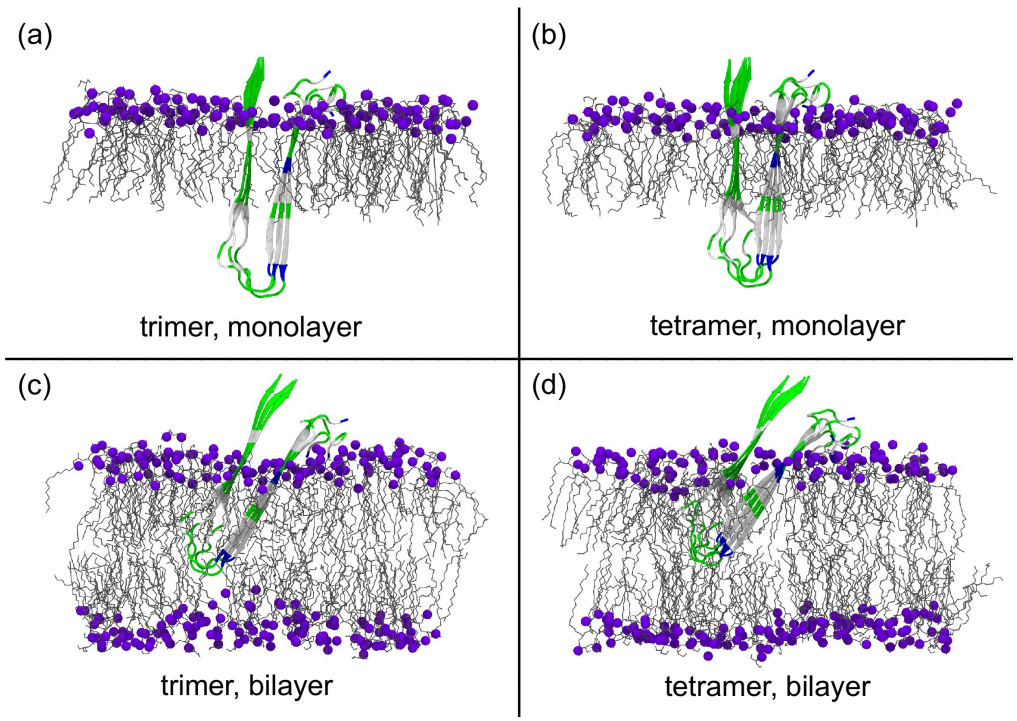

Figure S4: Starting structures showing the initial positions of hIAPP trimer and tetramer in both DPPG monolayer and bilayer.

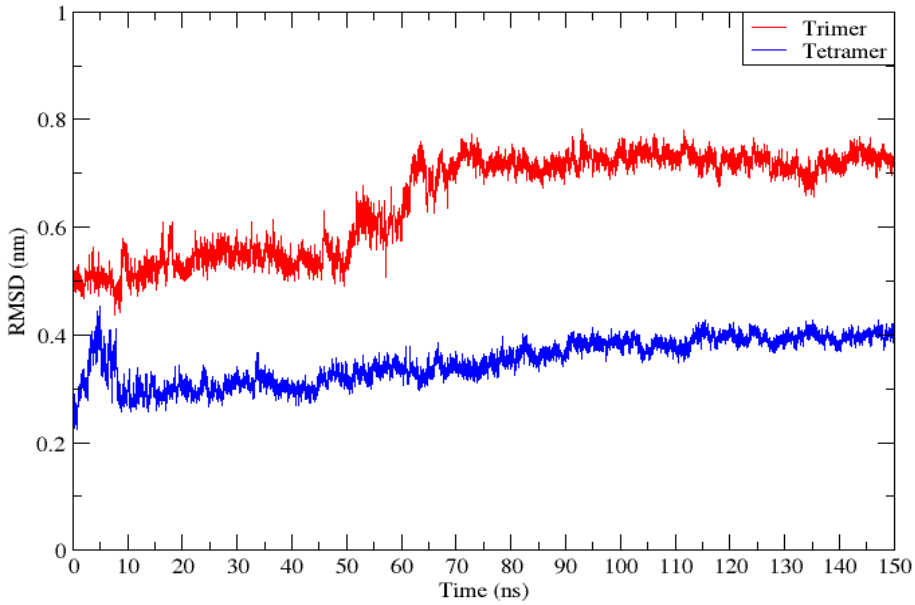

Figure S5: Backbone RMSD of hIAPP in DPPG monolayer.

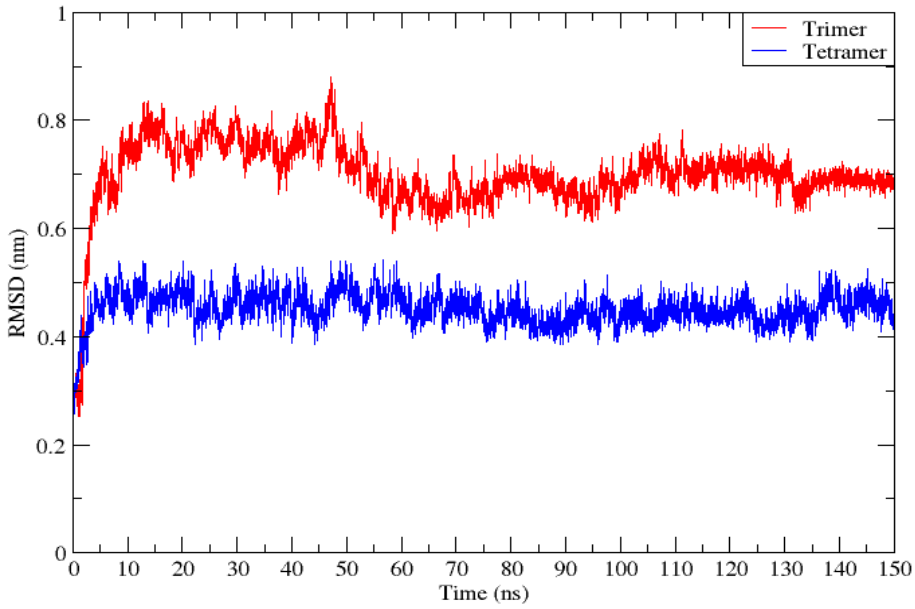

Figure S6: Backbone RMSD of hIAPP in DPPG bilayer.

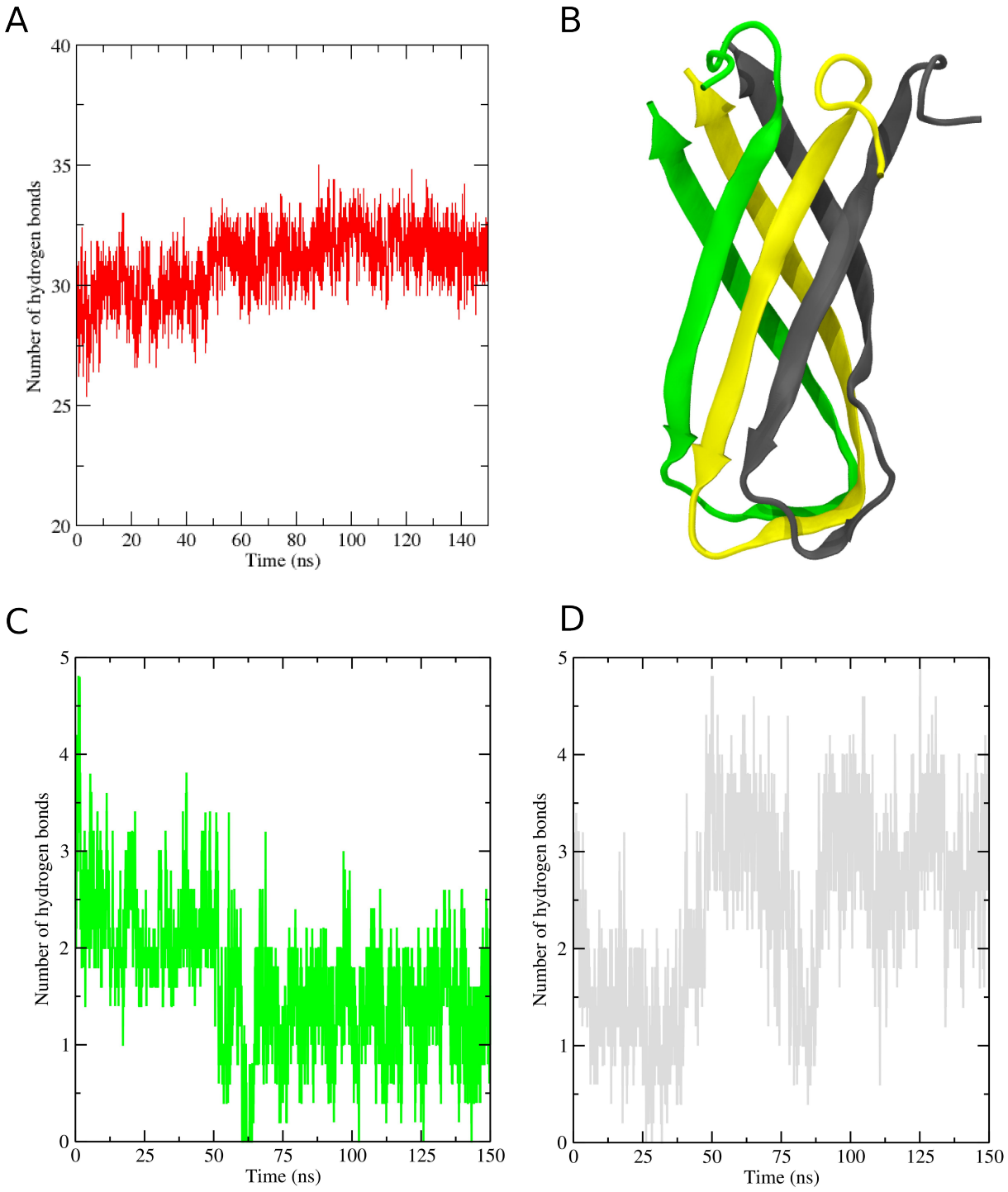

Figure S7: (a) Number of intra- and interpeptide hydrogen bonds in the hIAPP trimer in DPPG bilayer. (b) Most stable trimer structure colored by peptide numer (peptide 1, 2 and 3 in green, yellow and grey, respectively). (c) and (d) Number of H-bonds formed between the two β-sheets of peptide 1 (green) and peptide 3 (grey).

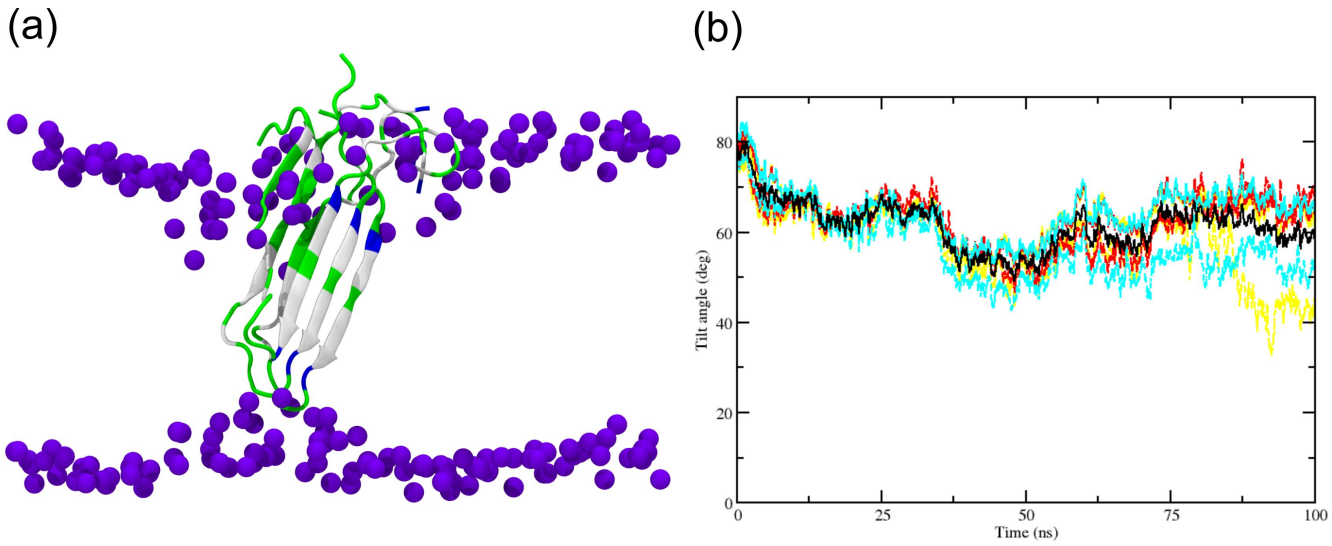

Figure S8: hIAPP trimer when inserted at 90^0 angle in a DPPG bilayer: (a) The most stable structure obtained from cluster analysis. (b) Average (dark line) and individual tilt angles of β strands relative to the membrane surface.

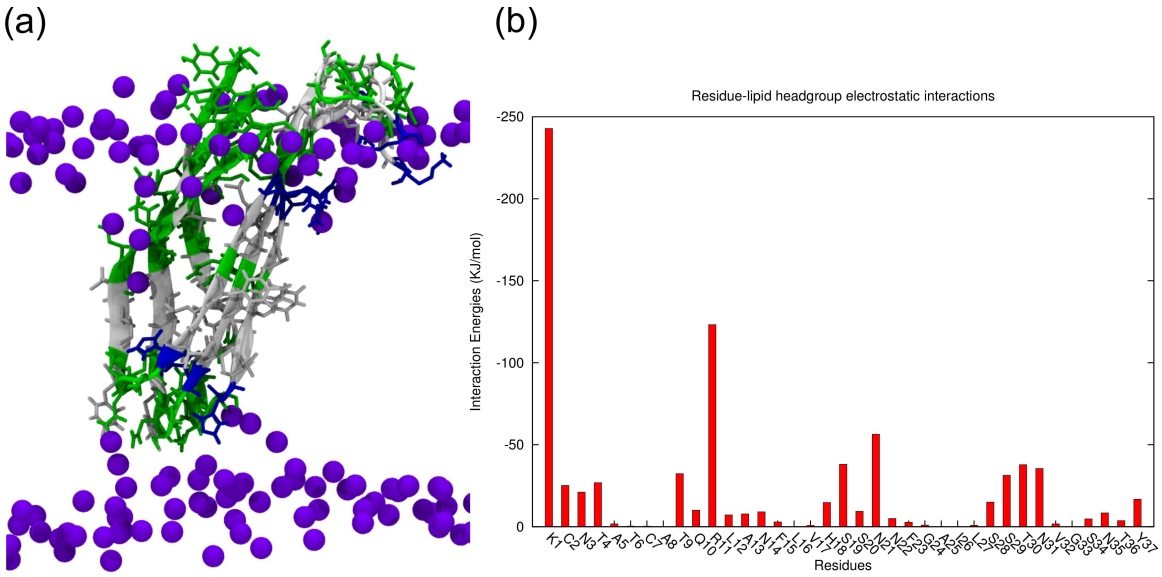

Figure S9: hIAPP trimer in a DPPG bilayer: (a) The most stable structure obtained from cluster analysis. The trimer side chains are shown as licorice. (b) Electrostatic interaction energies between the trimer residues and lipid headgroups. The interaction energies are averaged over three β strands.

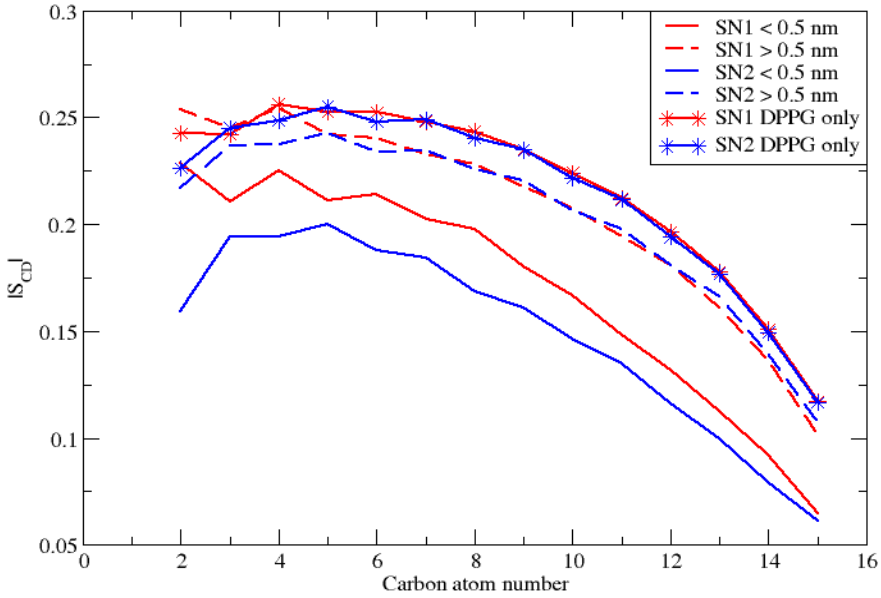

Figure S10: Time-averaged order parameter $|S_{CD}|$ of the sn-1 and sn-2 lipid chains resulting from the MD simulation of the hIAPP trimer in DPPG monolayer. S_{CD} is analyzed for lipids within 0.5 nm of protein and for lipids more than 0.5 nm away from protein. For comparison, $|S_{CD}|$ for lipids from the DPPG-only simulation is shown.

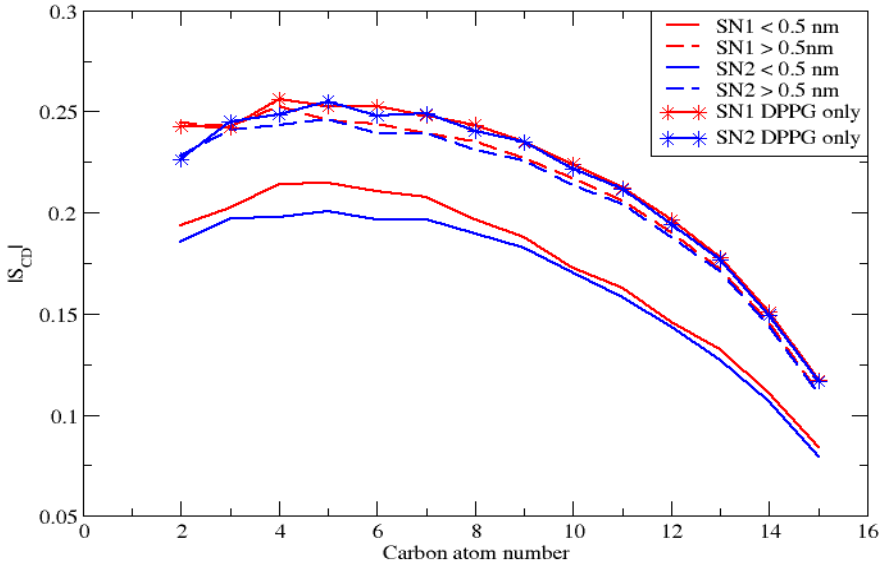

Figure S11: Time-averaged order parameter $|S_{CD}|$ of the sn-1 and sn-2 lipid chains resulting from the MD simulation of the hIAPP tetramer in DPPG monolayer. S_{CD} is analyzed for lipids within 0.5 nm of protein and for lipids more than 0.5 nm away from protein. For comparison, $|S_{CD}|$ for lipids from the DPPG-only simulation is shown.

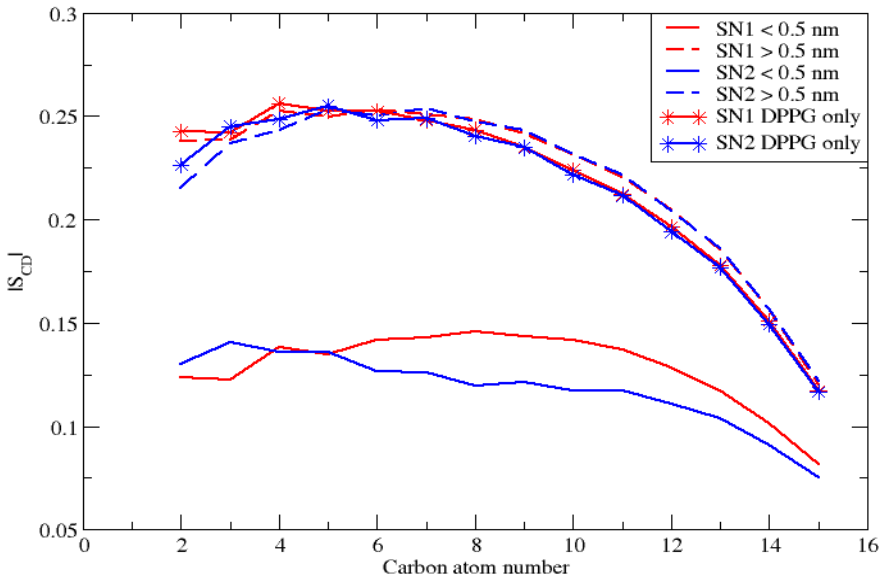

Figure S12: Time-averaged order parameter $|S_{CD}|$ of the sn-1 and sn-2 lipid chains resulting from the MD simulation of the hIAPP trimer in DPPG bilayer. S_{CD} is analyzed for lipids within 0.5 nm of protein and for lipids more than 0.5 nm away from protein. For comparison, $|S_{CD}|$ for lipids from the DPPG-only simulation is shown.

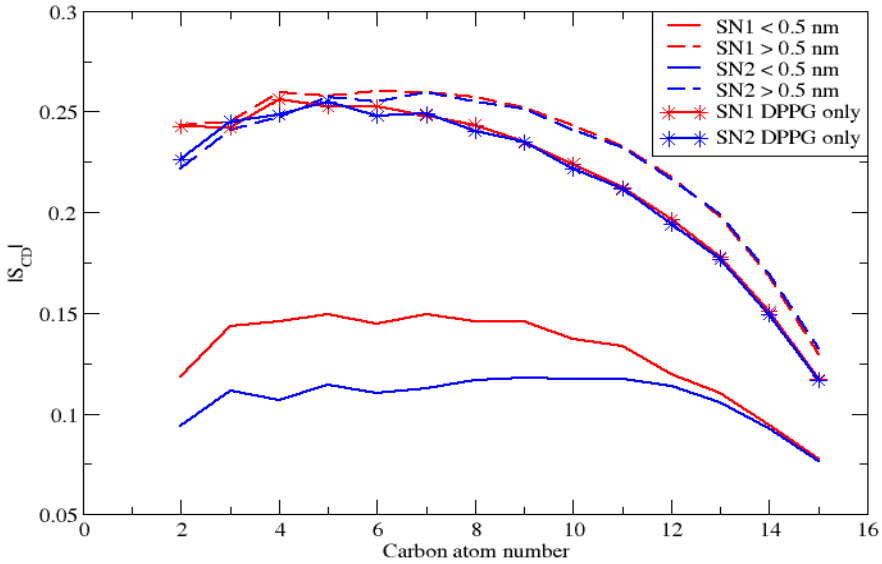

Figure S13: Time-averaged order parameter $|S_{CD}|$ of the sn-1 and sn-2 lipid chains resulting from the MD simulation of the hIAPP tetramer in DPPG bilayer. S_{CD} is analyzed for lipids within 0.5 nm of protein and for lipids more than 0.5 nm away from protein. For comparison, $|S_{CD}|$ for lipids from the DPPG-only simulation is shown.

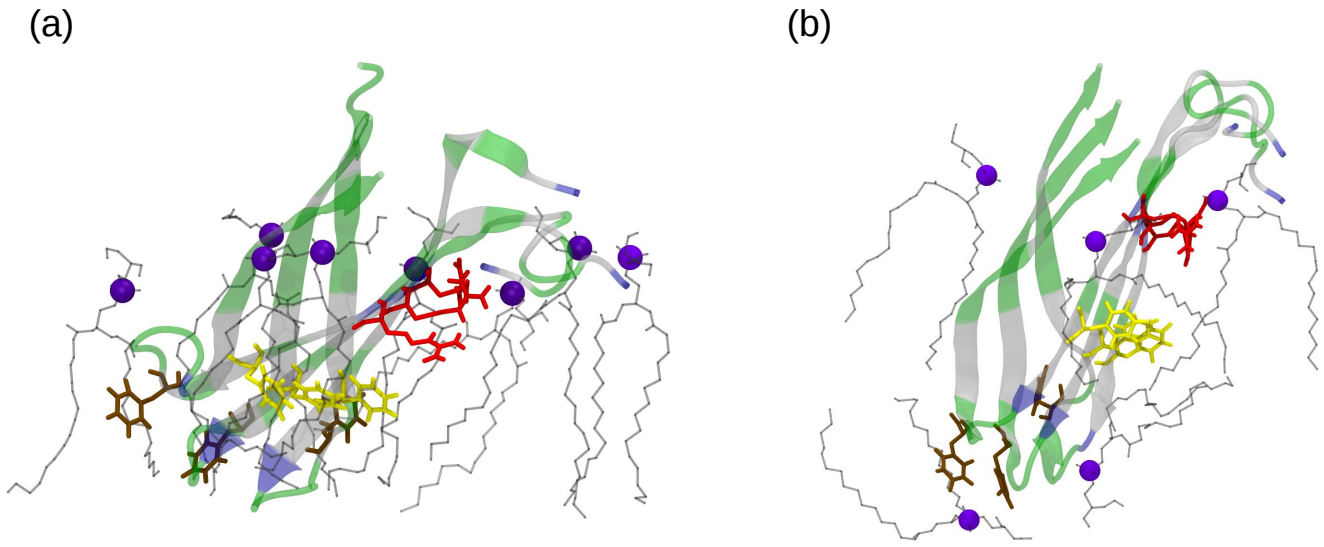

Figure S14: hIAPP trimer causing lipids in the (a) monolayer and (b) bilayer to tilt in the near vicinity of the peptides. The side chains with the strongest effect on acyl chain order are shown: Arg11 (red), Phe15 (yellow) and Phe23 (ochre).

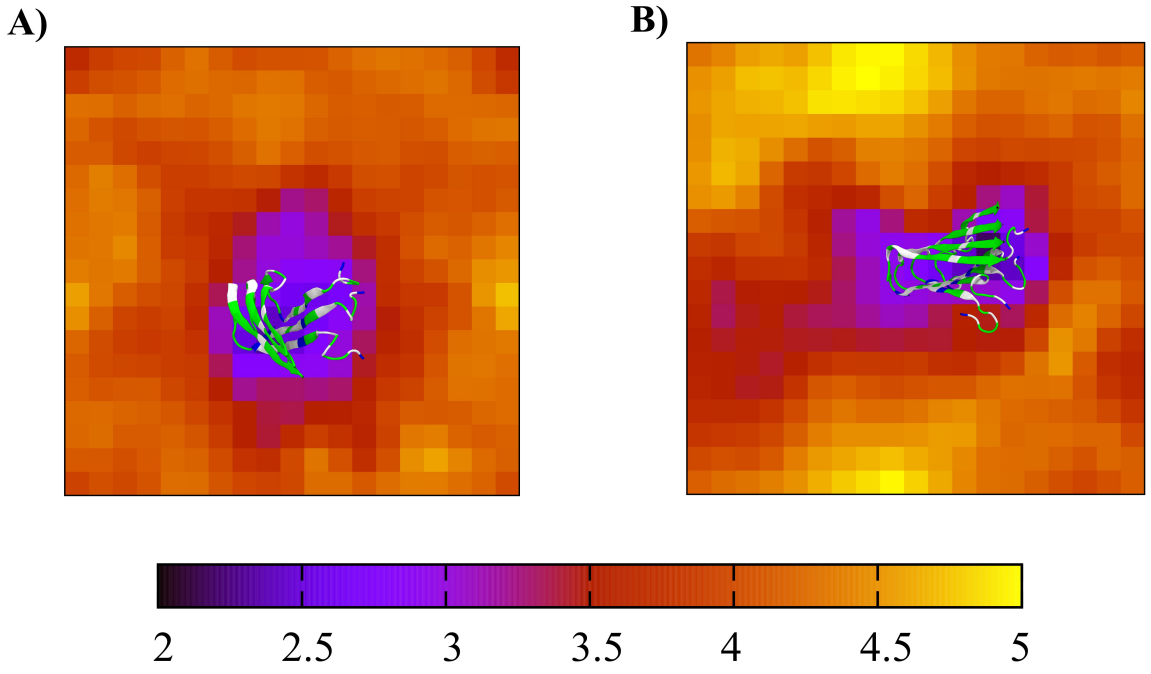

Figure S15: Bilayer thickness around embedded hIAPP for (a) trimer and (b) tetramer calculated for the final MD frame. For clarity, hIAPP was placed on the plots to indicate its position in the bilayer. The legend shows the bilayer thickness (nm) mapped to the corresponding colors.

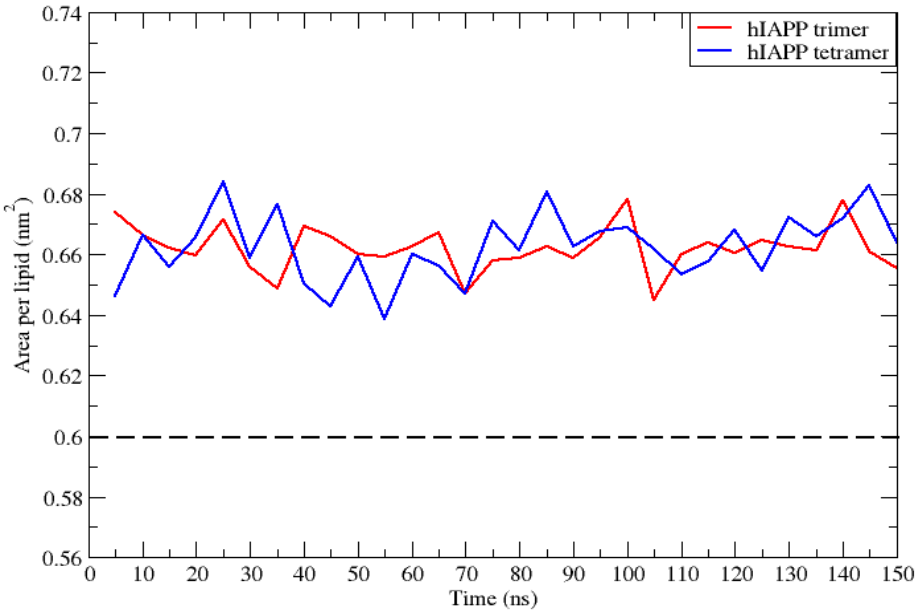

Figure S16: Area per lipid as a function of time for the DPPG monolayer simulations with hIAPP trimer (red) and tetramer (blue). For comparison, the average area per lipid obtained from a peptide-free DPPG bilayer is shown as black dashed line.

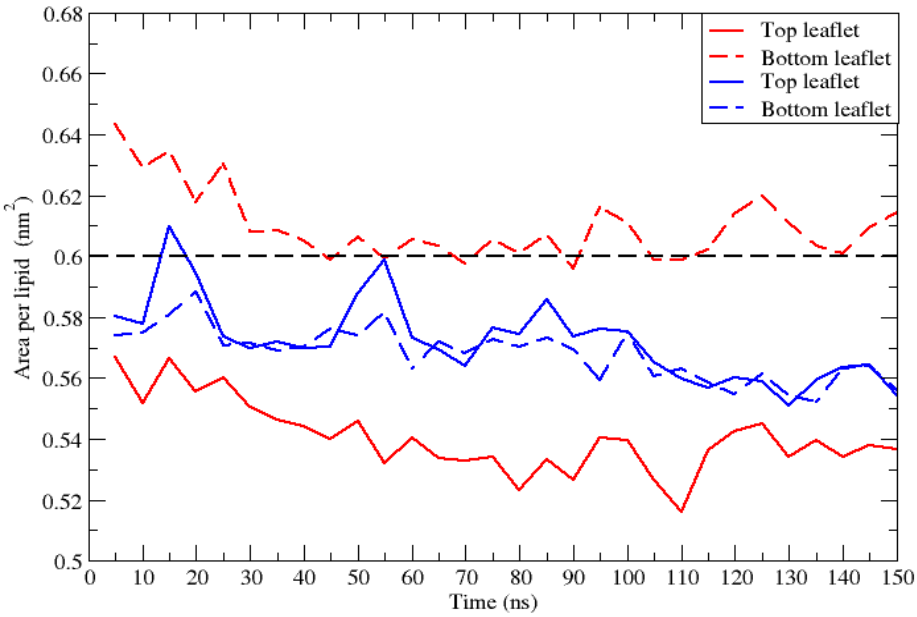

Figure S17: Area per lipid as a function of time for the DPPG bilayer simulations with hIAPP trimer (red) and tetramer (blue). For comparison, the average area per lipid obtained from a peptide-free DPPG bilayer is shown as black dashed line.

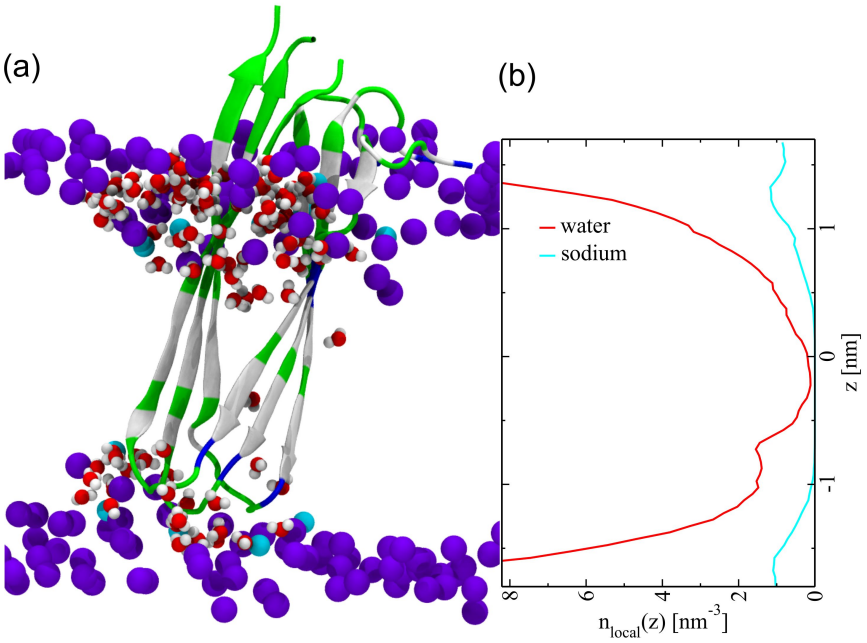

Figure S18: hIAPP trimer in a DPPG bilayer and 100 mM NaCl**:** (a) The most stable structure obtained from cluster analysis. The figure shows reduced water flow into the membrane and ions do not diffuse into the membrane hydrophobic core. Water molecules and Na^+ are shown as vdW spheres. (b) Averaged particle density of water and Na^+ within the the bilayer.

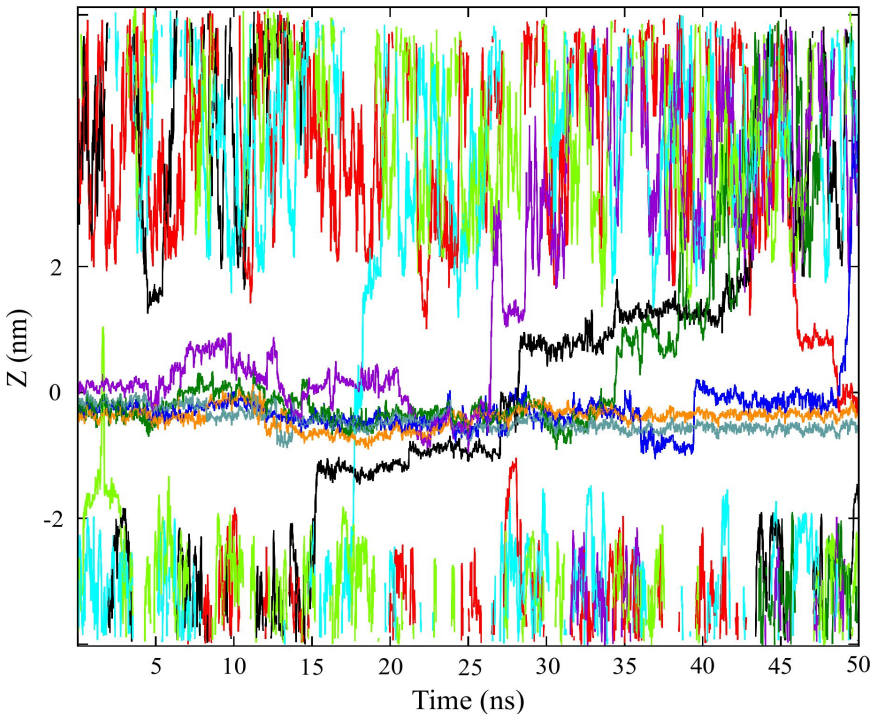

Figure S19: Representative trajectories of water molecules permeating the DPPG bilayer with hIAPP trimer inserted. Only the coordinate along the bilayer normal (*z*-axis) is plotted, and only permeation events occurring during the last 50 ns of the 150 ns MD simulation are shown.

Interaction energies [kJ/mol]	trimer/monolayer	tetramer/monolayer
hIAPP–hIAPP	-3104 ± 42	-3248 ± 37
hIAPP–lipid headgroups	-638 ± 95	-558 ± 47
hIAPP–water/ions	-1471 ± 90	-1419 ± 74
	trimer/bilayer	**tetramer/bilayer**
hIAPP–hIAPP	-3034 ± 43	-3166 ± 35
hIAPP–lipid headgroups	-1029 ± 49	-749 ± 66
hIAPP–water/ions	-1498 ± 68	-1397 ± 65

Table S1: Time and peptide averaged interaction energies and their standard deviations for the investigated systems. The energies were averaged over the last 100 ns of each MD trajectory. The energies, for which statistical relevant differences between trimer and tetramer can be observed, are highlighted in blue. The darker the highlighting, the larger the difference is.

SUPPORTING REFERENCES

1. Martinez, L., R. Andrade, E. G. Birgin, and J. M. Martinez, 2009. PACKMOL: A Package for Building Initial Configurations for Molecular Dynamics Simulations. *J. Comput. Chem*. 30:2157–2164.

2. Feller, S. E., Y. Zhang, and R. W. Pastor, 1995. Computer simulation of liquid/liquid interfaces. II. Surface tension–area dependence of a bilayer and monolayer. *J. Chem. Phys*. 103:10267–10276.

3. Kabsch, W., and C. Sander, 1983. Dictionary of protein secondary structure: Pattern recognition of hydrogen-bonded and geometrical features. *Biopolymers* 22:2577–2637.

4. Daura, X., K. Gademann, B. Jaun, D. Seebach, W. van Gunsteren, and A. Mark, 1999. Peptide folding: when simulation meets experiment. *Angew. Chem. Int. Ed*. 38:236–240.

5. Beckstein, O., and M. S. P. Sansom, 2004. The influence of geometry, surface character, and flexibility on the permeation of ions and water through biological pores. Phys. Biol. 1:42–52.

6. Allen, W. J., J. A. Lemkul, and D. R. Bevan, 2009. GridMAT-MD: A grid-based membrane analysis tool for use with molecular dynamics. *J . Comput. Chem.* 30:1952–1958.

7. Hub, J. S., H. Grubmüller, and B. L. de Groot, 2009. Dynamics and energetics of permeation through aquaporins. What do we learn from molecular dynamics simulations? *In* E. Beitz, editor, Aquaporins, Springer Berlin Heidelberg, volume 190 of Handbook of *Experimental Pharmacology*, 57–76.

8. Hub, J. S., F. K. Winkler, M. Merrick, and B. L. de Groot, 2010. Potentials of mean force and permeabilities for carbon dioxide, ammonia, and water flux across a rhesus protein channel and cipid membranes. *J. Am. Chem. Soc.* 132:13251–13263.

9. Moad, A. J., and G. J. Simpson, 2004. A unified treatment of selection rules and symmetry relations for sum-frequency and second harmonic spectroscopies. *J. Phys. Chem. B* 108:3548–3562.

10. Xiao, D., L. Fu, J. Liu, V. S. Batista, and E. C. Yan, 2012. Amphiphilic Adsorption of Human Islet Amyloid Polypeptide Aggregates to Lipid/Aqueous Interfaces. J. Mol. Biol. 421:537 – 547.